

# 1 **Common mode signals and vertical velocities in the great Alpine area**

## 2 **from GNSS data**

3 Francesco Pintori<sup>1</sup>, Enrico Serpelloni<sup>1,2</sup>, Adriano Gualandi<sup>1</sup>

4 <sup>1</sup>Istituto Nazionale di Geofisica e Vulcanologia (INGV), Osservatorio Nazionale Terremoti, Roma, 00143, Italy.

5 <sup>2</sup>Istituto Nazionale di Geofisica e Vulcanologia (INGV), Bologna, 40128, Italy.

6 *Correspondence to:* Francesco Pintori (francesco.pintori@ingv.it)

7 **Abstract.** We study the time series of vertical ground displacements from continuous GNSS stations located in the European  
8 Alps. Our goal is to improve the accuracy and precision of vertical ground velocities and spatial gradients across an actively  
9 deforming orogen, investigating the spatial and temporal features of the displacements caused by non-tectonic geophysical  
10 processes. We apply a multivariate statistics-based blind source separation algorithm to both GNSS displacement time series  
11 and to ground displacements modeled from atmospheric and hydrological loading, as obtained from global reanalysis models.  
12 This allows us to show that the retrieved geodetic vertical deformation signals are influenced by environmental-related  
13 processes and to identify their spatial patterns. Atmospheric loading is the most important one, reaching amplitudes larger than  
14 2 cm, but also hydrological loading, with amplitudes of about 1 cm, cause peculiar spatial features of GNSS ground  
15 displacements: while the displacements caused by atmospheric and hydrological loading are apparently spatially uniform, our  
16 statistical analysis shows the presence of NS and EW displacement gradients.

17 We filter out signals associated with non-tectonic deformation from the GNSS time series to study their impact on both the  
18 estimated noise and linear rates in the vertical direction. While the impact on rates appears rather limited, given also the long-  
19 time span of the time-series considered in this work, the uncertainties estimated from filtered time-series assuming a power  
20 law + white noise model are significantly reduced, with an important increase in white noise contributions to the total noise  
21 budget. Finally, we present the filtered velocity field and show how vertical ground velocity spatial gradients are positively  
22 correlated with topographic features of the Alps.

23  
24 **Summary** We study time varying vertical deformation signals in the European Alps by analyzing GNSS position time series.  
25 We associate the deformation signals to geophysical forcing processes, finding that atmospheric and hydrological loading are  
26 by far the most important cause of seasonal displacements. Recognizing and filtering out non-tectonic signals allows us to  
27 improve the accuracy and precision of the vertical velocities.

## 28 **1 Introduction**

29 The increasing availability of GNSS observations, both from geophysical and non-geophysical networks, pushed forward the  
30 use of ground displacement measurements to study active geophysical processes on land, ice and on atmosphere, with  
31 applications in a broad range of Earth science disciplines (e.g., Blewitt et al., 2018). Studies on active mountain building, in  
32 particular, can now benefit from the use of GNSS vertical ground motion rates to get new insights into the contribution of the  
33 different processes at work in the formation and evolution of mountain reliefs (e.g., Faccenna et al., 2014a; Sternai et al., 2019,  
34 Dal Zilio et al. 2021, Ching et al. 2011). Proposed mechanisms of rock uplift rate include isostatic adjustment to deglaciation,  
35 tectonic shortening, isostatic response to erosion and sediment redistribution, isostatic response to lithospheric structural  
36 changes and dynamic adjustment due to sub-lithospheric mantle flow (e.g., Faccenna et al., 2014b). All these processes sum-  
37 up to contribute to the actual vertical ground motion rates estimated from GNSS displacement time-series, and constraining  
38 their relative contribution to mountain dynamics is challenging, because of the different spatial and temporal scales involved  
39 and the short observational time period with respect to the characteristic timescales of the mentioned processes.

40 The availability of long-lasting (i.e., >8 yrs) GNSS position time-series minimizes the impact of transient and seasonal signals  
41 in the vertical rate estimates (Masson et al., 2019). However, it is worth considering that GNSS measurements record ground  
42 displacements due to a variety of multiscale processes (from continental-scale geodynamics and loading to local-scale  
43 hydrology and tectonics), resulting in the presence of several deformation signals superimposed on the main linear trend, which  
44 is commonly associated with geodynamic processes at the scale of current, decadal, geodetic observation window.

45 Excluding tectonic and volcanological processes, and once removed the effect of tides associated with solid earth, pole and  
46 ocean, variations of atmospheric pressure loading and fluid redistribution in the Earth crust are the main cause of vertical  
47 ground displacement recorded by GNSS stations worldwide (Liu et al. 2015). Atmospheric pressure and mass changes cause  
48 time-variable displacement because of the elastic response of the Earth surface to these load variations, with vertical  
49 displacements usually significantly larger than the horizontal ones, which appear as spatially-correlated signals with a  
50 dominant one year period (e.g., Fu and Freymueller, 2012; Fu et al., 2012). Seasonal displacements are also caused by non-  
51 tidal sea surface fluctuations. This process is of particular relevance in areas near the oceans, while in the inlands its effect is  
52 significantly reduced (van Dam et al., 2012).

53 The presence of spatially-correlated signals in GNSS time-series can result from either the aforementioned large scale  
54 processes, generally described as common mode signals (CMS), or processing errors, generally described as common mode  
55 error (CME), like the mismodeling of displacements caused by solid Earth, ocean and atmospheric, and satellite orbits  
56 mismodeling, which induces draconitic signals (Dong et al., 2006).

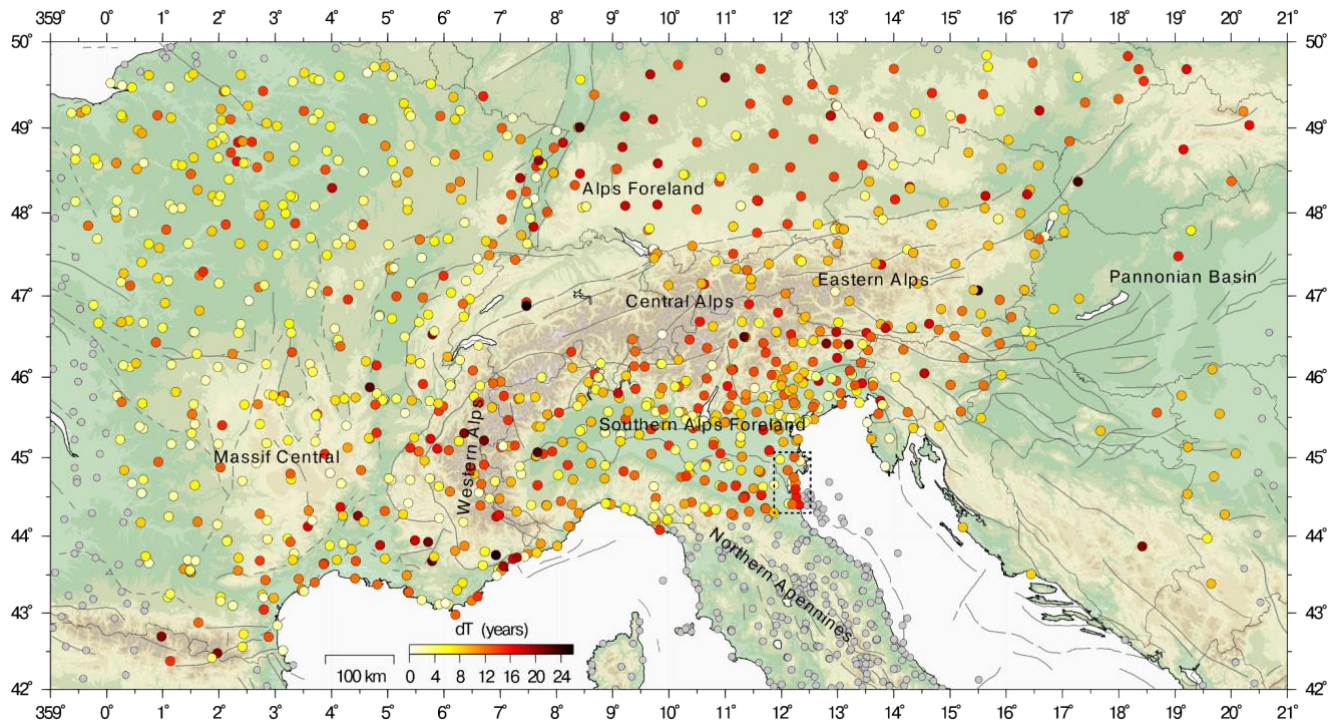
57 In the literature, the distinction between CMS and CME is not always clear, and spatially correlated signals are often removed  
58 from the time series as CME without attempts of interpretation (e.g., He et al., 2017; Hou et al., 2019; Serpelloni et al., 2013;  
59 Kreemer and Blewitt, 2021). Depending on the pursued goal, this approach can be fair. For example, if we were interested in  
60 the study of long-term linear deformation, we might consider CMS as CME, but it is worth noting that the “CME” definition

61 for signals clearly associated with geophysical processes might be misleading. The removal of the CME/CMS in GNSS  
62 position time-series, which is also known as time-series filtering, can help improve the precisions of the estimated linear  
63 velocities. Moreover, a better understanding of CMS/CME origin can also provide new information on other deformation  
64 mechanisms.

65 Here we use the European Alps as a natural laboratory to investigate the spatial and temporal contribution of different  
66 geophysical processes, which we identify through a variational Bayesian Independent Component Analysis (vbICA), on the  
67 vertical ground displacements recorded by a dense and spatially uniform network of continuous GNSS stations in the 2010-  
68 2020 time-span. The Alps represent the highest and most extensive mountain range of Europe (see Fig. 1). We focus on the  
69 vertical component, which is nominally less accurate and precise than the horizontal ones, because this mountain belt is  
70 characterized by significant ground uplift and spatial vertical velocity gradients that are correlated with topography (Serpelloni  
71 et al., 2013). The present-day convergence between Adria and the Eurasian plate is largely accommodated in the Eastern  
72 Southern Alps (e.g., Serpelloni et al., 2016) where the Adriatic lithosphere underthrusts the Alpine mountain belt, and here  
73 part of the observed vertical uplift is associated with active tectonics (Anderlini et al., 2020). Conversely, in other Alpine  
74 domains, positive vertical velocities most likely derive from a complex interplay of deep-seated geodynamic and isostatic  
75 processes (e.g., Sternai et al., 2019). In the Alpine framework, more accurate and precise measurements of geodetic vertical  
76 ground motion rates can provide new constraints on the dynamics contributing to the ongoing vertical rates and their spatial  
77 variations, with implications for the study of mountain building processes, response to deglaciation and active tectonics.

78 The structure of this work is as follows: in Section 2 we present methods commonly used for extracting spatially-correlated  
79 signals in GNSS time series; in Section 3 we describe the data and methods used in this work; in Section 4 we characterize the  
80 spatio-temporal behavior of three different independent datasets (GNSS vertical displacements, atmospheric and hydrological  
81 loading models displacement time series) applying on each of them a vbICA decomposition and studying how they are related.  
82 This allows us to spatially and temporally characterize the signals contributing to the measured GNSS displacement time series  
83 and associate them with geophysical processes. We also estimate the vertical velocities and the noise features of the GNSS  
84 stations after removing the non-tectonic signals identified with the vbICA analysis. In Section 5 we compare the results of  
85 different filtering methods and use the results of our time-series analyses in order to evaluate the effects of the signal filtering  
86 on the accuracies and precisions of the vertical velocities of the study region, which is of particular importance to better  
87 characterize the processes generating the Alps uplift.

88



89

90 **Figure 1: Map of the study area showing the location of GNSS stations. Coloured circles show GNSS stations considered in the time-**  
 91 **series analysis, with colours representing the length of the time-interval for which data are available at each station (0-25 years).**  
 92 **The grey circles show GNSS stations not included in the time-series analysis to reduce contamination of deformation processes not**  
 93 **associated with the Alps. Dark grey lines represent mapped faults from the Geodynamic Map of the Mediterranean. The dashed box**  
 94 **includes GNSS stations affected by anthropogenic deformation signals (Palano et al., 2020).**

## 95 2 Methods for the spatially-correlated signals extraction in GNSS time series

96 Two widely used techniques for extracting CMS from a GNSS network are the Stacking Filtering Method (SFM, Wdowinski  
 97 et al., 1997) and the Weighted Stacking Filtering Method (WSFM, Nikolaidis, 2002), which differs from the first because of  
 98 a weighting factor based on the uncertainty associated with the GNSS data at each epoch.

99 Examples of time series filtering with the WSFM are provided by Ghasemi Khalkhali et al. (2021) in Northwest Iran, Jiang et  
 100 al. (2018) in California and by Zhang et al. (2020) in China. The networks of the aforementioned studies span less than 1000  
 101 km. However, when considering networks covering larger areas, the assumption that the CMS has uniform spatial distribution  
 102 throughout the network is not valid (Dong et al., 2006; Tian and Shen, 2016; Ming et al., 2017), and the stacking methods  
 103 become imprecise.

104 To take into account spatial heterogeneities, Tian and Shen (2016) propose an alternative stacking approach: the Correlation-  
 105 Weighted Spatial Filtering (CWSF) method. Unlike the SFM, CWSF includes the spatial variability of CMS through a

106 weighting factor, which depends on the correlation coefficient between the residual position time series and on the distance  
107 between the stations. Zhu et al. (2017) use CWSF to estimate the CMS on the Crustal Movement Observation Network of  
108 China and discuss the effects of the thermal expansion and environmental loading, which includes atmospheric pressure  
109 loading, non-tidal ocean loading and continental water storage. They find that while vertical CMS are mainly associated with  
110 environmental loading, thermal expansion plays a minor role.

111 A filtering method similar to CWSF, called CMC Imaging, is developed and used by Kreemer and Blewitt (2021) in western  
112 Europe to extract common mode components that are as local as possible. The main difference between CWSF and CMC  
113 Imaging is that the former uses as a weighting factor both the distance and the correlation coefficient among the stations, while  
114 the latter only the correlation coefficient, showing that it is representative of the distance among the stations. While the authors  
115 do not explore the nature of the extracted CMS, they show that the CMC Imaging method is very effective in filtering out  
116 CMS from GNSS time series, increasing the accuracy and precision of the velocity estimation. In particular, they show that  
117 the minimum length of a time series needed to retrieve the long term velocity, within a given confidence limit, is almost halved  
118 after the filtering.

119 Multivariate statistical techniques like Principal Component Analysis (PCA) and Independent Component Analysis (ICA) are  
120 filtering techniques based on a completely different approach than stacking. Since they allow to take into account for the spatial  
121 variability of CMS (Dong et al. 2006), ICA and PCA are used to characterize and interpret them. Multivariate statistics  
122 techniques are also applied to study spatially-correlated seasonal displacements, which have been the target of several  
123 researches in the last few years.

124 In California, Tiampo et al. (2004) associate a seasonal signal, extracted through the Karhunen-Loeve expansion technique,  
125 with the combined effect of groundwater and pressure loading. In Taiwan, Kumar et al. (2020) find a close relationship between  
126 atmospheric loading and CMS, extracted using a PCA; while Liu et al. (2017) apply a ICA to show that in the Nepal Himalaya  
127 region annual vertical displacements are associated with atmospheric and hydrological loading.

128 Yuan et al. (2018) use three Principal Components (PCs) for CMS filtering over China, because of the presence of spatial  
129 gradients related to the large extension of the study region. In that work, the authors show that environmental loading is one  
130 of the sources of the CMS and that vertical GNSS velocities uncertainties are significantly reduced (54%) after CMS filtering.

131 Pan et al. (2019) find that the precision of the GNSS velocities, especially in the vertical component, increases after removing  
132 spatially-correlated signals related to draconitic errors and to climate oscillation (La Niña - El Niño). The spatially-correlated  
133 signals are identified by applying a PCA to the GNSS time series, where the linear trend and the seasonal signals are removed.  
134 Pan's work is a good example of how vertical displacements are more affected by climate-related processes and data processing  
135 errors than the horizontal ones, demonstrating that the vertical component is particularly worth analyzing with care.

136 The application of the ICA also proved effective for time series filtering, as shown by Hou et al. (2019): they identify spatially-  
137 correlated signals and even though they do not provide an interpretation, classifying them as CME, they show that the precision  
138 of the time series significantly increases after the filtering by ICA. Liu et al. (2015) use both PCA and FastICA algorithms

139 (Hyvärinen and Oja, 1997) to extract and interpret CMS as caused by atmospheric and soil moisture loading in the UK and the  
140 Sichuan-Yunnan region in China.

141 Other examples of the influence of the non-tectonic processes on vertical velocity estimation are provided by Riddell et al.  
142 (2020), who study the vertical velocities of the GNSS stations in Australia to estimate the contribution of the glacial isostatic  
143 adjustment. One of the results of Riddell's work is the reduction of the vertical velocity uncertainty, achieved by first subtracting  
144 the displacements associated with atmospheric, hydrological and non-tidal ocean loading from the GNSS time series, and then  
145 filtering the residuals by applying both PCA and ICA.

146 The vbICA is a multivariate statistics-based blind source separation algorithm (Choudrey, 2002) implemented by Gualandi et  
147 al. (2016) for solving the problem of blind source separation of deformation signals in GNSS position-times series and has  
148 been successfully used to extract tectonic and hydrological transient deformation signals in (e.g., Gualandi et al., 2017a;  
149 Gualandi et al., 2017b; Serpelloni et al., 2018). Larochelle et al. (2018) applied vbICA to study the relationship between GNSS  
150 and Gravity Recovery and Climate Experiment (GRACE)-derived displacements in Nepal Himalaya and Arabian Peninsula,  
151 with the goal of extracting seasonal signals and identifying the processes that generate them. Serpelloni et al. (2018) and Pintori  
152 et al. (2021) use vbICA to characterize hydrological deformation signals associated with the hydrological cycle at a spatial  
153 scale not resolvable by GRACE observations, separating ground water storage signals from other surface mass loading signals;  
154 while Silverii et al. (2021) perform a vbICA decomposition on GNSS time series in the Long Valley Caldera region (California,  
155 USA) to separate volcanic-related signals from other deformation processes, in particular the one associated with hydrology.  
156 This method is also recently applied to InSAR data (Gualandi and Liu, 2021) to estimate the displacement caused by sediments'  
157 compaction in San Joaquin Valley (California) and to separate a seasonal signal from the tectonic loading in the Central San  
158 Andreas Fault zone.

### 159 **3 Data and Methods**

#### 160 **3.1 GNSS dataset and time-series analysis**

161 Over the European plate, in particular, GNSS networks managed by national and regional agencies, provide a rather uniform  
162 spatial coverage (e.g., <https://epnd.sgo-penc.hu/> and <https://gnss-epos.eu/>). Figure 1 shows the distribution of continuous  
163 GNSS stations operating across the great Alpine area where, excluding Switzerland for which raw observations are not  
164 accessible, GNSS stations cover, rather uniformly, both the mountain range and the European and Adriatic forelands. We  
165 analyze the raw GPS observations using the GAMIT/GLOBK (Ver. 10.71) software (Herring et al, 2018), following the  
166 standard procedures of the repro2 IGS reprocessing scheme (<http://acc.igs.org/reprocess2.html>). This is part of a large  
167 processing effort, including >4000 stations in the Euro-Mediterranean and African region, where sub-networks, made by <50  
168 stations, dynamically and optimally selected based on daily data availability, are processed independently with GAMIT and  
169 later tied together using common, sub-net, tie sites and IGB14 core-stations, using the GLOBK software. The details of the  
170 processing are given in the Supplementary Information S1. The result of our analysis is a set of ground displacement time-

171 series, realized in the IGB14 reference frame (<ftp://igs-rf.ign.fr/pub/IGb14>). The resulting position time-series (hereinafter  
172 IGB14-time series) have been then analyzed in order to estimate, and correct, instrumental offsets due to changes in the station's  
173 equipment setup, as extracted from sitelog or RINEX file headers.

174 We consider the vertical displacement time-series of the stations between longitude  $0^{\circ}$ - $21^{\circ}$  and latitude  $42^{\circ}$ - $50^{\circ}$ N (see coloured  
175 circles in Fig. 1) in the 2010-2020 time-span, excluding the sites in the northern Adriatic coast, known to be affected by  
176 anthropogenic deformation signals (dashed box in Fig. 1) due to gas extraction (Palano et al., 2020) and the stations located in  
177 the northern and central Apennines, where other tectonic and geodynamic processes are going on. We focus on the last decade,  
178 in order to have the most uniform set of continuous measurements possible in, at least, a 10 years time-span. We acknowledge  
179 that some of the stations shown in Fig. 1 have much longer time-series, but this time-interval maximizes the number of  
180 simultaneous observations at many stations.

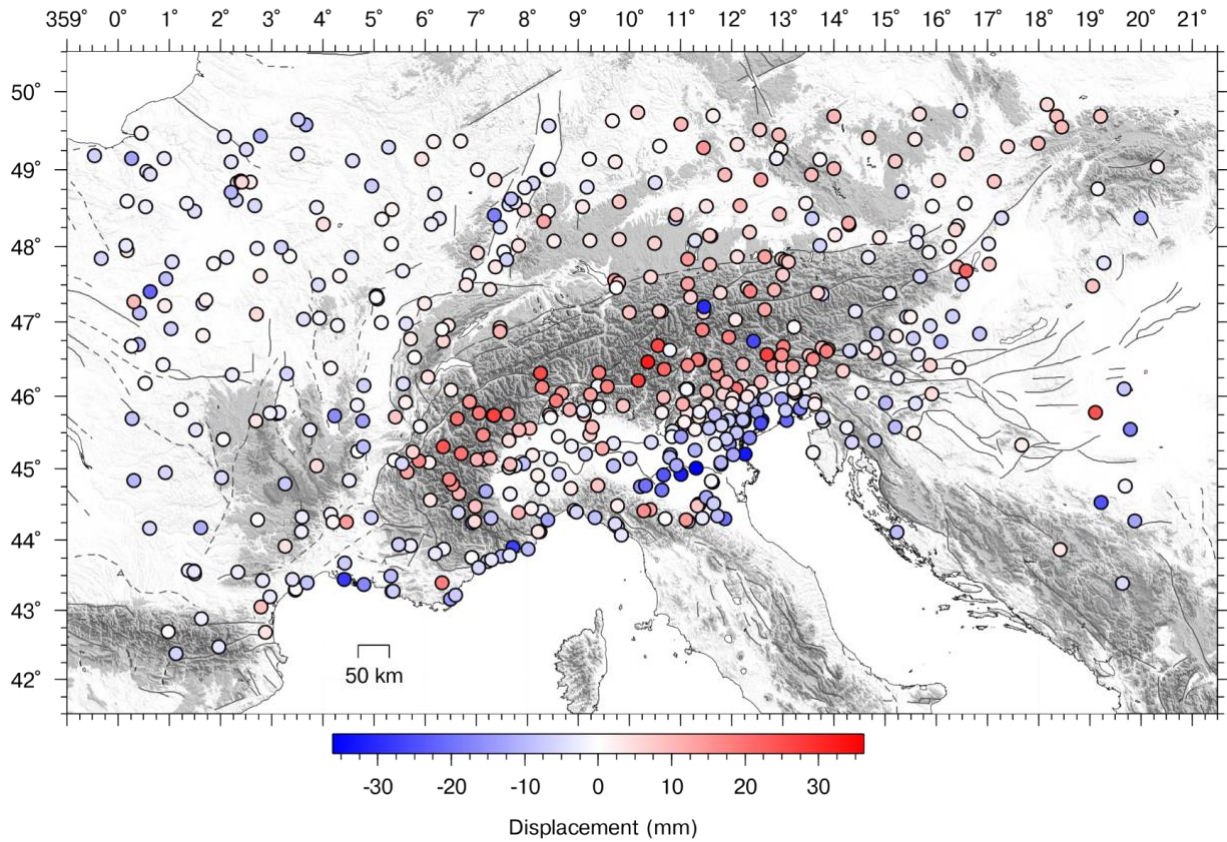
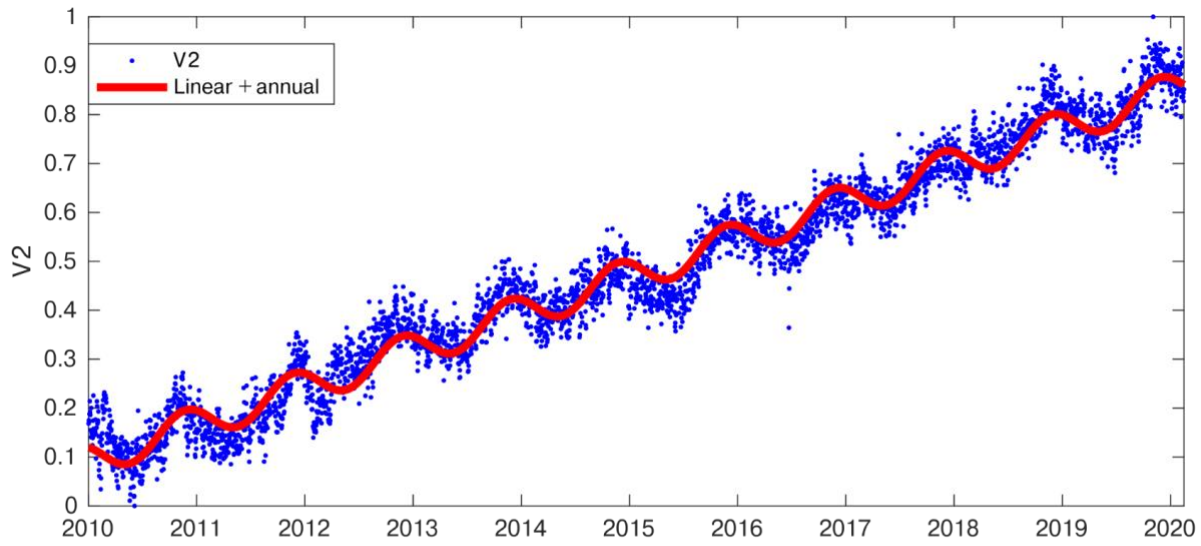
181 The IGB14 vertical displacement time-series are analyzed with the blind source separation algorithm based on vbICA  
182 (Choudrey and Roberts, 2003; Gualandi et al., 2016). This technique falls under the umbrella of the so-called unsupervised  
183 learning approaches, and it aims at finding statistically independent patterns that can be linearly combined to reconstruct the  
184 original dataset. Differently from other commonly used ICA approaches, like for example FastICA (Hyvarinen and Oja, 1999),  
185 the adopted vbICA is a modeling approach that uses a mix of Gaussians to reproduce the probability density functions (PDFs)  
186 of the underlying sources. The variational Bayesian approach introduces an approximating PDF for the posterior parameters  
187 of the model, and the cost function to be maximized is the Negative Free Energy of the model, which can be explicitly  
188 calculated once a specific form for the approximating posterior PDF is chosen. This framework is particularly advantageous  
189 because it allows for more flexibility in the description of the sources' PDF, giving the chance to model multimodal  
190 distributions and to take into account missing data in the input time series.

191 The input time-series contains a secular motion, roughly representing the vertical rate in the IGB14 reference frame, which is  
192 superimposed by a variety of signals, of different temporal and spatial signatures. The first step of our analysis is to estimate  
193 a linear component to represent the secular motion and remove it from the time series. This is required by the fact that the  
194 vbICA is more effective in separating the sources when the temporal correlation in the dataset is low. Here, rather than using  
195 a classic trajectory model (e.g., Bevis and Brown, 2014) to model and detrend the original time-series, in order to avoid biases  
196 in the estimates of station velocities due to the short length of the time series and to the possible presence of strong nonlinear  
197 signals, we take this step in a multivariate sense as in Pintori et al. 2021. We perform a first ICA decomposition considering 8  
198 components (or ICs). The number of components is determined by applying an F-test to establish if a more complicated model  
199 is supported by the data at a 0.05 significance level (Kositsky and Avouac, 2010). The results of this analysis are reported in  
200 Fig. S1, and show that one component, nominally IC2, contains a linear trend, with some cross-talk with a seasonal (annual)  
201 signal, as shown in Fig. 2.

202 Before discussing the vbICA results, we briefly explain how to interpret the temporal evolution and the spatial distribution of  
203 the ICs, so that it is possible to retrieve the displacements associated with them. The color of each GNSS site in Fig. 2 represents  
204 the IC2 spatial response ( $U_2$ ), which indicates the maximum displacement associated with the IC2, while the temporal function

205 V2 is normalized between 0 and 1. The displacement associated with IC2 between two epochs (e.g.  $t_1$  and  $t_2$ , with  $t_2 > t_1$ ) at the  
206 station  $n$  is computed as  $V1(t_2) * U1_n - V1(t_1) * U1_n(t_1)$ , where  $V1(t_2)$  is the value associated with the temporal evolution of the IC  
207 at the epoch  $t_2$ .  $U1_n$  depends on the site, but not on the epoch; its unit of measurement is mm, while  $V$  has no units of  
208 measurement. As a result,  $V1 * U1_n$  is in mm. It follows that if  $U1_n$  is positive, as we observe for each station, and  $V1$  is  
209 increasing ( $V1(t_2) > V1(t_1)$ ), the stations move upward during the  $t_2 - t_1$  time interval. On the other hand, if  $V1(t_2) < V1(t_1)$  the  
210 stations move downward during  $t_2 - t_1$ . As regards Fig. 2, assuming  $t_1 = 2010.0$  and  $t_2 = 2020.0$ , the displacements associated with  
211 IC2 are  $\sim 30$  mm upward at the “red” GNSS stations,  $\sim 30$  mm downward at the “blue” GNSS stations and  $\sim 0$  mm at the white  
212 ones.





213

214

**Figure 2: Temporal evolution and spatial response of the IC2 of the GNSS decomposition. Time series have been corrected only for instrumental offsets.**

215

216

217 We fit a linear trend to the temporal evolution of IC2 (V2) using the function

218

$$219 \quad V2(t) = q + m \cdot t + A \cdot \sin(2\pi \cdot t + \varphi) \quad (1)$$

220

221 Once estimated  $m$  and  $q$  from (1) via a non-linear least square approach, we compute the displacements associated with IC2,  
222 considering as its temporal evolution the function  $y=q + m \cdot t$ ; then, we remove the computed displacements from each  
223 original, IGB14, time series, obtaining the detrended dataset used in the subsequent decomposition step. The advantage of this  
224 approach, compared to a trajectory model, is that it is not necessary to assume any temporal evolution of the deformation  
225 signals a priori, except for the limited number of functions that make up Eq. (1). This is particularly advantageous in cases  
226 where either transients of unknown origin or amplitude and/or phase fluctuations of the seasonalities are affecting some stations  
227 and could lead to a mismodeling by a trajectory model. Notice in particular how signals potentially biasing the linear trend,  
228 like the multi-annual ones in case of short time series, are separated from the IC representing the stations' velocities.

229 The results of the vbICA applied to the detrended time-series are shown and discussed in Sect. 4.1.

### 230 **3.2 Meteo-climatic datasets**

231 The results of the decomposition of the geodetic dataset are compared with the results obtained from the analysis of  
232 displacement time-series associated with different meteo-climate forcings. In particular, here we consider hydrological,  
233 atmospheric loading and precipitation from global, gridded, models. These time-series are analyzed with the vbICA method  
234 already used for the geodetic dataset, and the results are compared in Sect. 3.2.

235 The Land Surface Discharge Model (LSDM), developed by Dill (2008), simulates global water storage variations of surface  
236 water in rivers, lakes, wetlands, and soil moisture, as well as from water stored as snow and ice. The LSDM is forced with  
237 precipitation, evaporation, and temperature from an atmospheric model developed by the European Centre for Medium-Range  
238 Weather Forecasts (ECMWF). Using the Green's function approach, Dill and Dobslaw (2013) compute daily surface  
239 displacements at  $0.5^\circ$  global grids caused by LSDM-based continental hydrology (hereinafter HYDL), and by non-tidal  
240 atmospheric surface pressure variations (hereinafter NTAL). We also considered the *École et observatoire des sciences de la*  
241 *terre* (EOST) loading service, which provides a model for the atmospheric and hydrological loading induced displacements.  
242 Ground displacements are computed using the Load Love Numbers estimate from a spherical Earth model (Gegout et al.,  
243 2010). The atmospheric loading is modeled using the data of the ECMWF surface pressure, assuming an Inverted Barometer  
244 ocean response; the hydrological loading includes soil moisture and snow height estimated from the Global Land Data  
245 Assimilation System (GLDAS/Noah; Rodell et al., 2004). All the datasets we have considered are provided in the center of  
246 figure reference frame, have daily temporal resolution and spatial resolution of  $0.5^\circ$ . It is worth noting that neither LSDM-  
247 based nor EOST models consider deep groundwater variations. GRACE data are often used to study hydrologically-induced  
248 deformation associated with groundwater; in fact, through the analysis of the gravity field variations, it is possible to retrieve

249 changes through time of the water masses. GRACE has the advantage of being influenced by groundwater variations, which  
250 are not taken into account by the HYDL model, but at the cost of a lower temporal (i.e., monthly) and spatial (~300 km)  
251 resolution.

252 The precipitation data we use are provided by the NASA Goddard Earth Sciences Data and Information Services Center  
253 (Huffman et al., 2019), they are daily with a spatial resolution of 0.1°.

## 254 **4 Results**

### 255 **4.1 Decomposition of GNSS time-series**

256 Figure 3 shows the result of the vbICA decomposition on the detrended displacement time-series, using 7 components as  
257 suggested by the F-test.

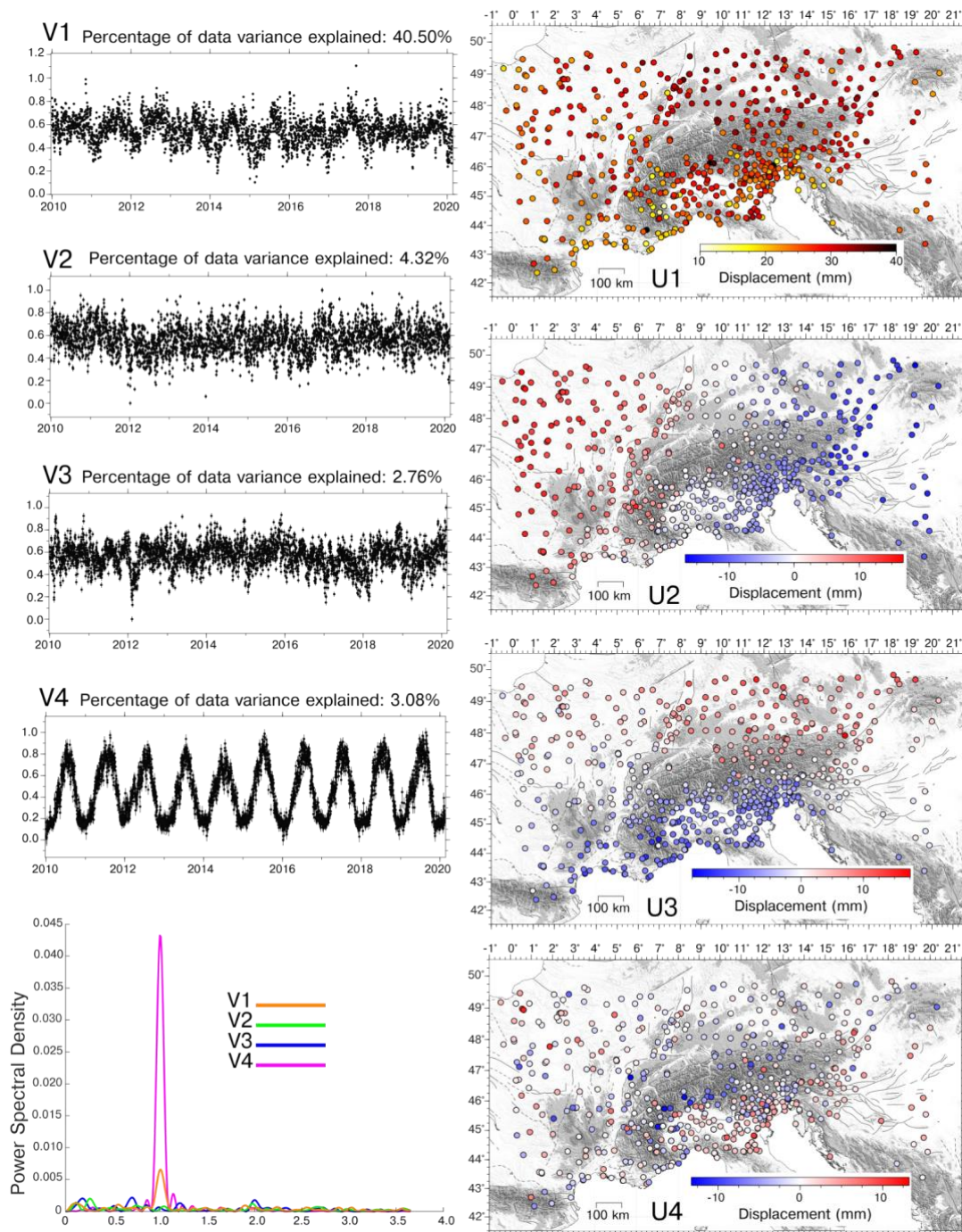
258 IC1 is a spatially uniform signal characterized by an annual temporal signature, as shown by the power spectral density (PSD)  
259 plot in Fig. 3a.

260 The mean of the maximum amplitudes is 26 mm, while the histogram showing the distribution of displacement amplitudes is  
261 shown in Fig. S4a.

262 IC2 shows a spatial response characterized by a clear E-W gradient, but, differently from IC1, its temporal evolution has not  
263 a dominant frequency. The spatial response U2 of the eastern stations (in blue) is mainly negative, while the U2 of the western  
264 stations (in red) is mainly positive. This means that when V2 is increasing the western (red) stations move up, while the eastern  
265 (blue) ones move down. The sites in the central portion of the study area (in white) are very slightly affected by the IC2  
266 component. The features of IC3 are analogous to those of the IC2, with the exception that a N-S gradient is present. The mean  
267 of the amplitude of the absolute value of IC2 spatial distribution is 6.7 mm; and it is 5.6 mm for IC3. The histogram showing  
268 the distribution of the absolute value is shown in Fig. S4b and S4c.

269 IC4 is an annual signal, as IC1, but with a heterogeneous spatial response: while some stations move upward some others  
270 move downward. The mean of the amplitudes absolute value of the displacements is 2.7 mm; the relative histogram is shown  
271 in Fig. S4d. The distribution of stations displaced with this phase difference seems to be mostly affected by geographical  
272 features: the stations located in mountain regions subside when V3 increases, whereas the stations far from relief move upward.  
273 The remaining three components are likely associated with local processes and discussed in the Supplementary Information  
274 S3.

275



276  
277  
278

**Figure 3: Temporal evolution, power spectral density and spatial response of: a) IC1; b) IC2; c) IC3; d) IC4.**

## 279 4.2 GNSS vs environmental-related displacements

280 As discussed in the introduction, atmospheric and hydrological loading are likely the main sources of vertical displacement in  
281 the great Alpine region. Since they are both uniform in terms of spatial response, showing smooth spatial variations, we decided  
282 to check if the first 3 ICs of the GNSS decomposition are associated with the displacements due to atmospheric and  
283 hydrological loading, and with their pattern of variability.

284 The vbICA analysis separates the data into statistically independent signals, which is useful because independent signals are  
285 often caused by different and independent sources of deformation. Nonetheless, a single source of deformation, such as  
286 atmospheric or hydrological loading, can be spatially heterogeneous and characterized by peculiar spatio-temporal patterns. In  
287 this case, the vbICA separates a single source of deformation in different components associated with different spatio-temporal  
288 patterns. As a consequence, we decided to apply a vbICA decomposition on HYDL and NTAL model displacement time series  
289 in order to check if they show any pattern and if they resemble the spatial distribution of IC1, IC2 and IC3 of the GNSS  
290 decomposition. NTAL and HYDL data have not been detrended.

291 We analyze with vbICA the hydrological loading (HYDL) and atmospheric pressure (NTAL) induced ground displacement  
292 models (EOST and LSDM-based), in order to characterize the spatial pattern and temporal response associated with these  
293 deformation sources, and study any possible link with the geodetic deformation signals described in Sect. 4.1. We use the  
294 results of the global models to estimate the hydrological loading, even though we are aware that some local effects might not  
295 be captured. In fact, considering the extension of the study area, it is very complicated to take into account the local features  
296 needed to estimate the hydrological loading with a better precision than the one provided by the global models.

297 In particular, in this section we show the results obtained using the LSDM-based models because they take into account the  
298 water stored in rivers, lakes and wetlands, while the EOST models do not. The results obtained using the EOST models are  
299 presented in the Supplementary Information S2. Figure 4 and 5 show the spatial response, the temporal evolution and the PSD  
300 of the ICs obtained using three components, to the NTAL (4) and HYDL (5) ground displacements. We decided to use three  
301 components to reproduce the displacement patterns of IC1, IC2 and IC3 of the GNSS decomposition.

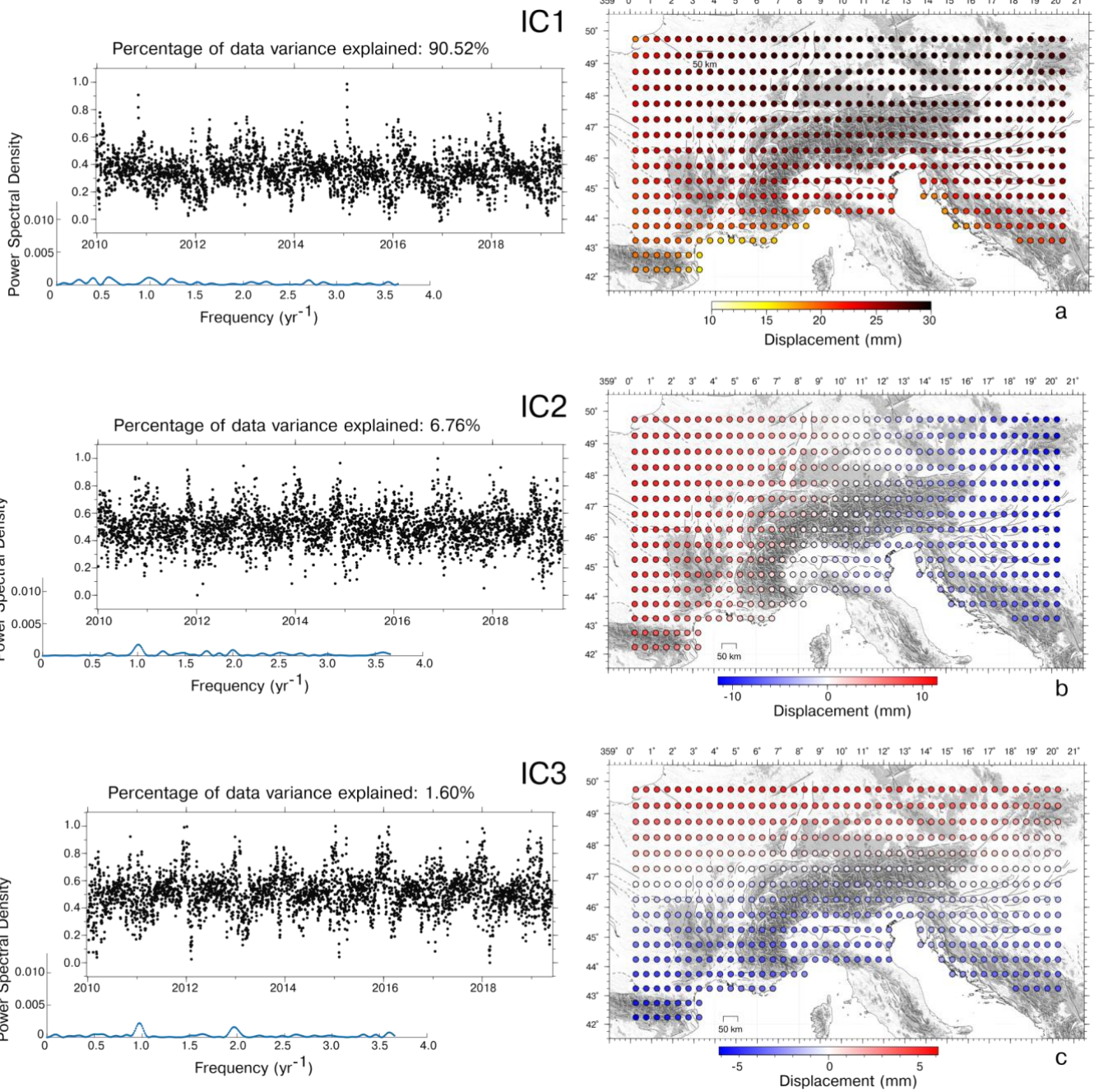
302 The first IC of both NTAL and HYDL shows a uniform spatial response, as IC1 of the GNSS dataset (Fig. 3a). The  
303 mean/median amplitude of the maximum displacements associated with NTAL is very similar to GNSS both in terms of  
304 mean/median amplitude (Table S1a) and distribution (Fig. 6, a); while for the HYDL model the amplitude is about two times  
305 smaller than NTAL.

306 IC2 and IC3 of both NTAL and HYDL show E-W and N-S gradients in the spatial response, respectively, as observed for IC2  
307 and IC3 of the GNSS dataset (Fig. 3b, d). Since the ICs spatial response of the NTAL and HYDL decomposition are very  
308 similar, we also consider the sum of the displacement associated with NTAL and HYDL models, which can be considered as  
309 “environmental loading”: we use the notation NTAL+HYDL\_ICn to indicate the sum of the displacement associated with the  
310 n-th component of the NTAL and HYDL decomposition. The amplitude of NTAL+HYDL\_IC1, NTAL+HYDL\_IC2 and

311 NTAL+HYDL\_IC3 are only slightly lower than the ones of GNSS\_IC1, GNSS\_IC2 and GNSS\_IC3, as shown in Fig. 6  
312 (panels g,h,i) and in Table S1a.

313 Concerning the temporal evolutions, IC1 of the HYDL model is an annual signal, while the IC2 and IC3 PSD plots indicate  
314 the presence of multi-annual signals. Unlike the HYDL decomposition, all the ICs of the NTAL decomposition contain the  
315 annual frequency, in particular IC2, whereas IC3 also contains semiannual ones. It is also worth noting that the temporal  
316 evolution of the ICs associated with the NTAL model are much more scattered than the ones resulting from HYDL, clearly  
317 indicating that the displacements due to atmospheric pressure variations can show large fluctuations at daily timescale.

318 We also perform a vbICA decomposition on both datasets using two and four components, presented in the Supplementary  
319 Information (Fig. S6 and S7). When using only two ICs, the results obtained (Fig. S6) are very similar to the first two ICs of  
320 the 3-components decomposition. The first three ICs of the four component decompositions (Fig. S7) have both temporal  
321 evolution and spatial distribution very similar to what is shown in Fig. 4 and Fig. 5. IC4 of the NTAL model has an annual  
322 signature and a E-W gradient with a shorter wavelength compared to IC2, while IC4 of the HYDL decomposition has a NW-  
323 SE gradient. This suggests that the N-S and E-W spatial patterns associated with the meteoroclimatic datasets are a robust feature,  
324 being insensitive to the number of components chosen in the decomposition. It is also worth noting that the decompositions of  
325 the NTAL and HYDL models explain the 98.89% and the 97.03% of the total variance when using 3 ICs, suggesting that  
326 increasing the number of the ICs is not necessary. As a result, in the following discussion we refer to the results obtained from  
327 the 3-components decomposition using the LSDM-based models, but remember that the results obtained using the EOST  
328 models are fully comparable (Supplementary Information S2).



329

330

**Figure 4: Temporal evolution, power spectral density and spatial response of IC1, IC2, IC3 of the NTAL model.**

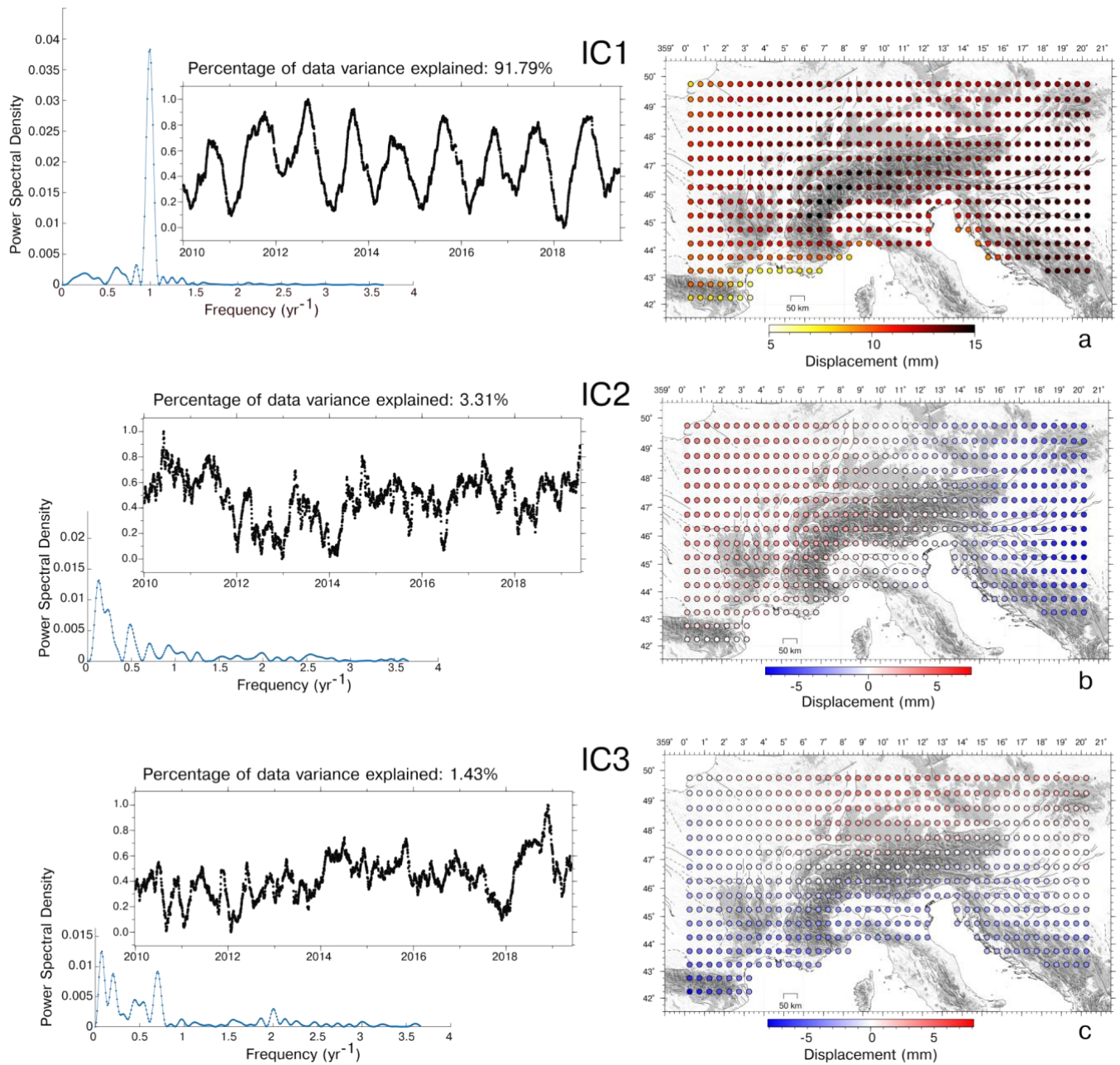
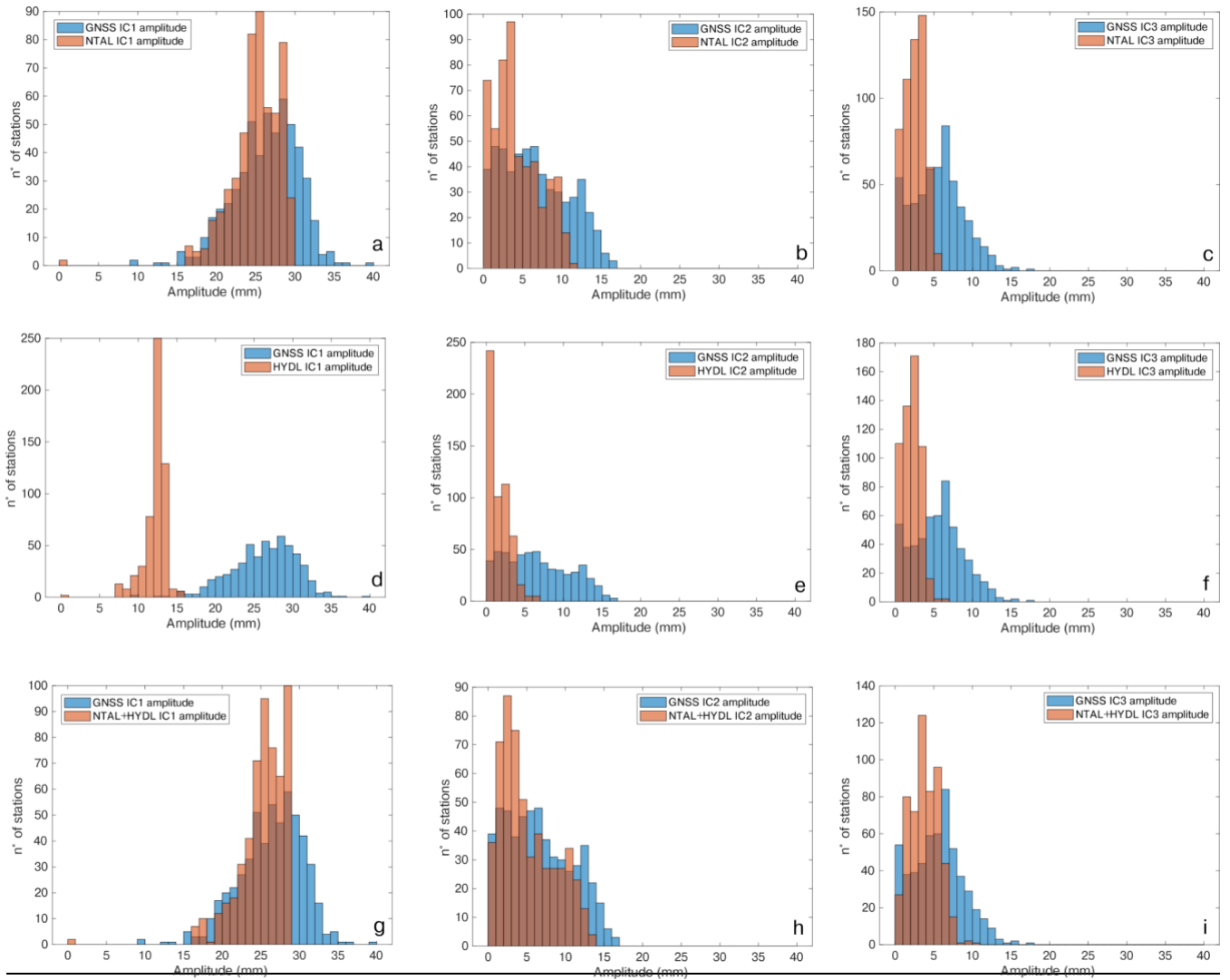


Figure 5: Temporal evolution, power spectral density and spatial response of IC1, IC2, IC3 of the HYDL model.

331  
332  
333  
334





335  
 336 **Figure 6. Histogram of the maximum displacements associated with:**  
 337 **(a) IC1 of the NTAL decomposition (orange), compared with the IC1 of the GNSS decomposition (blue); (b) same as (a) but**  
 338 **considering IC2; (c) same as (a) but considering IC3;**  
 339 **(d) IC1 of the HYDL decomposition (orange), compared with the IC1 of the GNSS decomposition (blue); (e) same as (d) but**  
 340 **considering IC2; (f) same as (d) but considering IC3;**  
 341 **(g) IC1 of the NTAL+HYDL decomposition (orange), compared with the IC1 of the GNSS decomposition (blue); (h) same as (g) but**  
 342 **considering IC2; (i) same as (g) but considering IC3.**

343  
 344 In order to quantify the agreement between the displacements associated with the hydrological and atmospheric pressure  
 345 loading and the ICs of the GNSS dataset displaying consistent spatial patterns (IC1, IC2, IC3), we compute, for each GNSS  
 346 station, the Lin concordance correlation coefficient (Lin, 1989) between the displacement reconstructed by the ICs associated

347 with the different LSDM-based models. Unlike Pearson's correlation coefficient, Lin's one takes into account similarities on  
348 both amplitudes and shapes of two time series.

349 The IC1 of the GNSS decomposition (GNSS\_IC1) is compared with the first component of both NTAL (NTAL\_IC1) and  
350 HYDL (HYDL\_IC1) datasets by associating each GNSS site with the nearest grid-point where NTAL and HYDL  
351 displacements are computed.

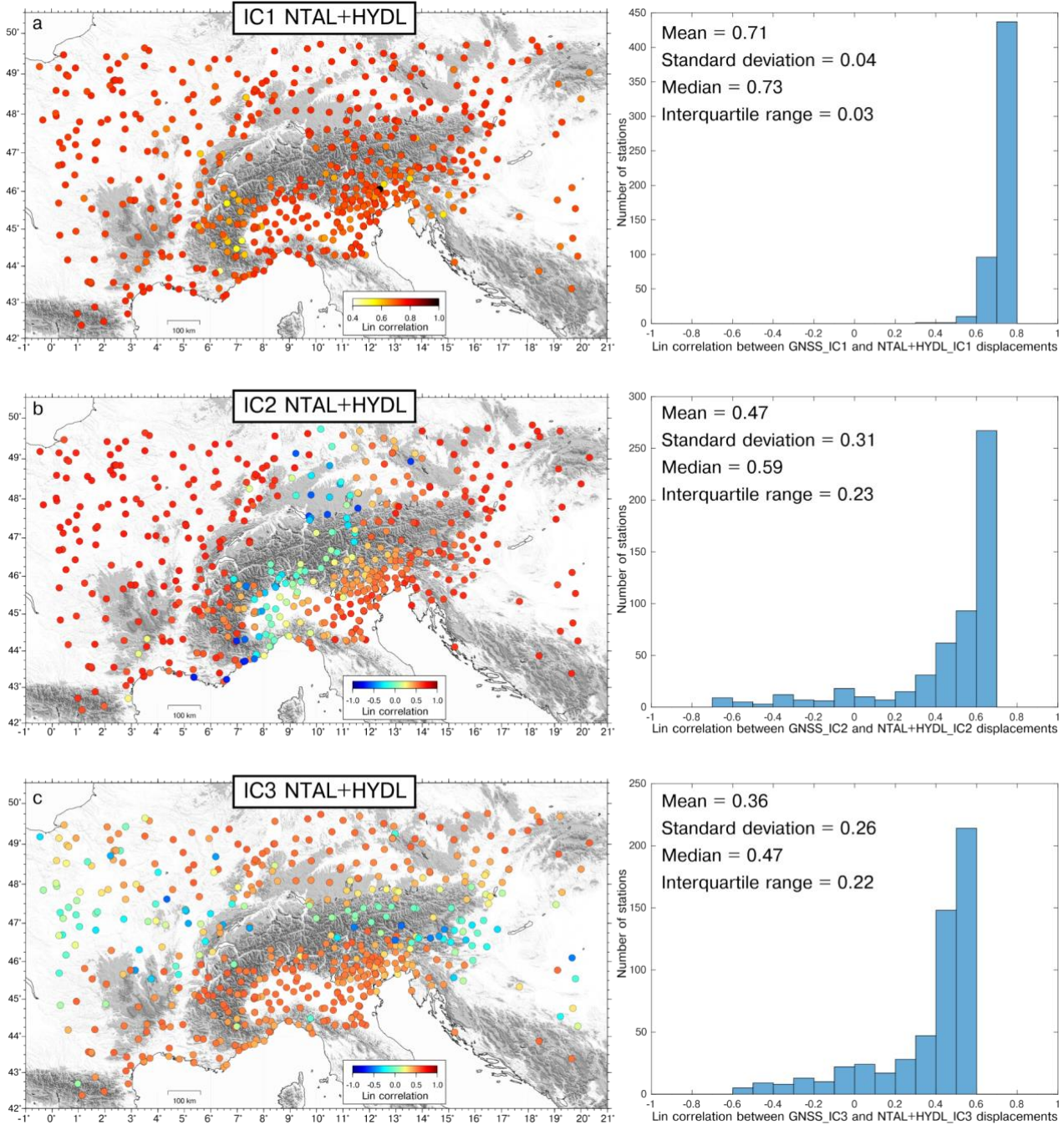
352 When considering the NTAL\_IC1, we observe (Fig. S8a) a high temporal correlation with GNSS\_IC1, while the correlation  
353 between GNSS\_IC1 and HYDL\_IC1 is significantly lower (Fig. S9a). In both cases the value of the Lin correlation coefficient  
354 is quite uniform in the dataset ( $\sim 0.59$  for NTAL\_IC1 and  $\sim 0.35$  for HYDL\_IC1). The Pearson correlation is similar to Lin's  
355 one (0.60 for NTAL\_IC1 and 0.35 for HYDL\_IC1), indicating that the amplitude of both NTAL\_IC1 and HYDL\_IC1 is  
356 similar to the GNSS\_IC1 amplitude. It is worth noting that if we consider NTAL+HYDL\_IC1, the correlation with GNSS\_IC1  
357 increases to  $\sim 0.73$  (Fig. 7a). As a result, we can interpret GNSS\_IC1 as the combined contribution of NTAL and HYDL, where  
358 NTAL plays the dominant role.

359 When considering IC2, we observe similar correlations between GNSS\_IC2 and either NTAL\_IC2 or HYDL\_IC2 (Fig. S8b,  
360 S8b). Nonetheless, in this case the correlation patterns are less uniform than the IC1 case, and few stations are even negatively  
361 correlated with both NTAL\_IC2 and HYDL\_IC2 displacements. The sites where GNSS\_IC2 displacements are negatively or  
362 weakly correlated with NTAL\_IC2 are the ones with the lowest IC2 amplitude. In fact, if we consider the stations whose  
363 maximum displacements associated with GNSS\_IC2 are larger than 3 mm, which are 411 out of 545, their mean Lin correlation  
364 with NTAL\_IC2 is 0.52; while the stations with amplitudes smaller than 3 mm have a mean correlation of 0.17. This is due to  
365 the fact that, given the low displacements associated at these stations, the correlation is more sensitive to noise. The agreement  
366 between the GNSS\_IC2 and NTAL\_IC2 is also confirmed by the Pearson correlation coefficient between the temporal  
367 evolution of the two ICs, which is 0.63; while the Pearson correlation between GNSS\_IC2 and HYDL\_IC2 is 0.28. The same  
368 pattern is observed when comparing GNSS\_IC2 with NTAL+HYDL\_IC2 (Fig. 7b): using 3 mm as threshold between large  
369 and small GNSS\_IC2 maximum displacements, the mean correlation is 0.57 for the stations most affected by this signal and  
370 0.14 for the remaining ones. This suggests that also GNSS\_IC2 is likely related to NTAL and HYDL loading processes.

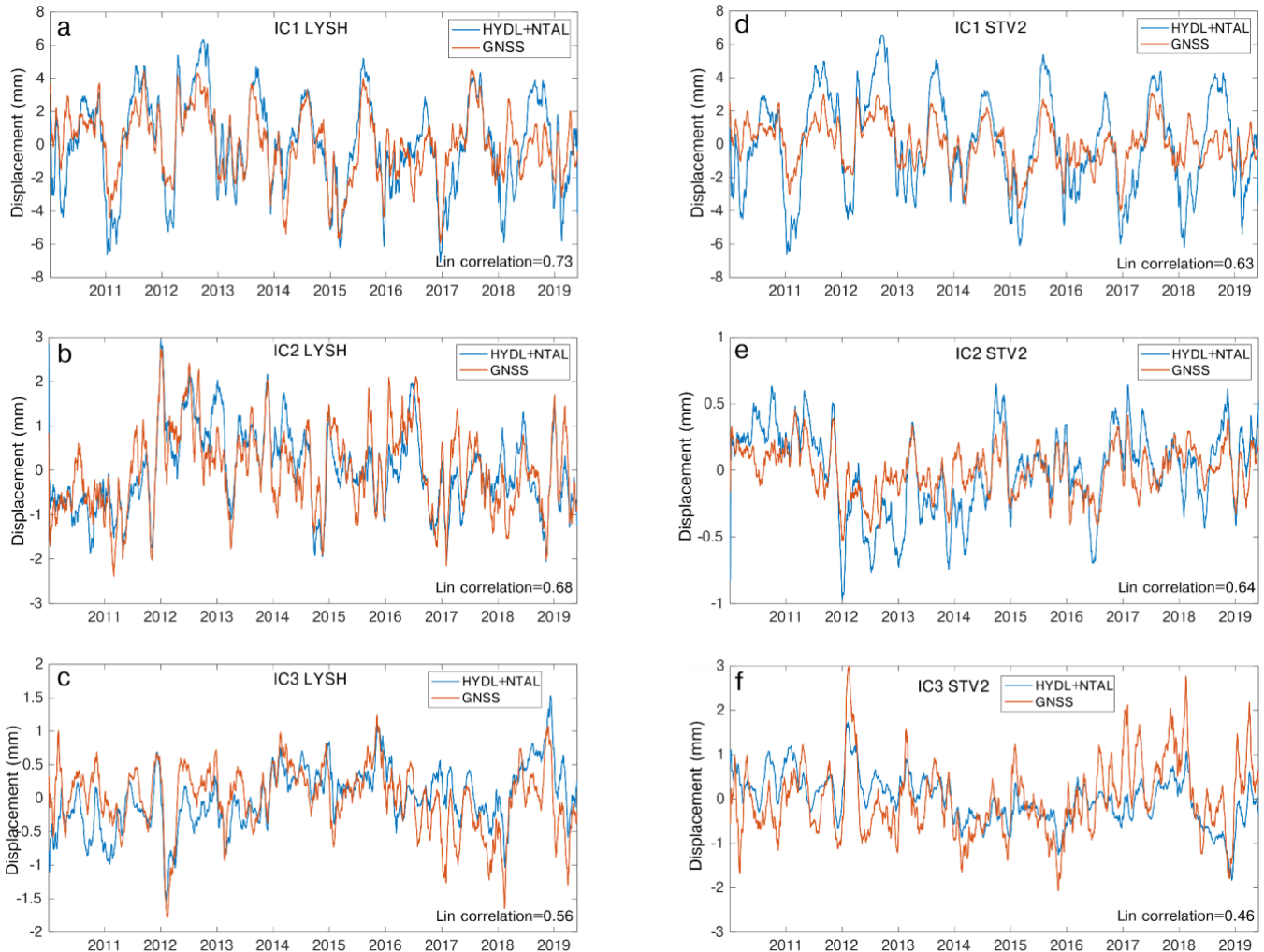
371 The Lin correlation between GNSS\_IC3 and NTAL+HYDL\_IC3 resembles what just shown for IC2 (Fig. 7c): at sites where  
372 the GNSS\_IC3 maximum amplitude is larger than 3 mm, which are 414 out of 545, the mean correlation with  
373 NTAL+HYDL\_IC3 is 0.44; while it is 0.10 for the remaining ones. As for IC1, both GNSS\_IC2 and IC3 displacements are  
374 best reproduced when considering the combined effect of NTAL and HYDL (see Fig. S8c, S9c compared to Fig. 7). The  
375 Pearson correlation between GNSS\_IC3 and NTAL\_IC3 is 0.47; while between GNSS\_IC3 and HYDL\_IC3 is 0.30.

376 To summarize, the three common mode signals components of the GNSS decomposition (IC1, IC2, IC3) are likely due to the  
377 combined effect of the atmospheric and hydrological loading. Due to the similarity between the spatial response of  
378 displacements associated with these two processes, it is possible that the vbICA technique is not able to separate them in the  
379 geodetic data; nonetheless, it highlights their spatial variability through IC2 and IC3.

380 Examples of comparison between climate-related displacements reconstructed at two different sites and the GNSS  
 381 decomposition are shown in Fig. 8.



382  
 383 **Figure 7: Lin correlation coefficients between: a) GNSS-IC1 and NTAL+HYDL\_IC1; b) GNSS\_IC2 and NTAL+HYDL\_IC2; c)**  
 384 **GNSS-IC3 and NTAL+HYDL\_IC3. Histograms of the correlation coefficients are also reported.**



387

388

389

390

391

**Figure 8: Comparison, at the LYSH (Lon: 18.45°; Lat: 49.55°) site, between the displacements associated with: a) GNSS\_IC1 and NTAL+HYDL\_IC1; b) GNSS\_IC2 and NTAL+HYDL\_IC2 ; c) GNSS\_IC3 and NTAL+HYDL\_IC3. d), e), f) are the same as a), b), c), respectively, for the STV2 (Lon: 6.11°; Lat: 44.57°) site. A 30-days moving average filter is applied to better visualize the data.**

392

393

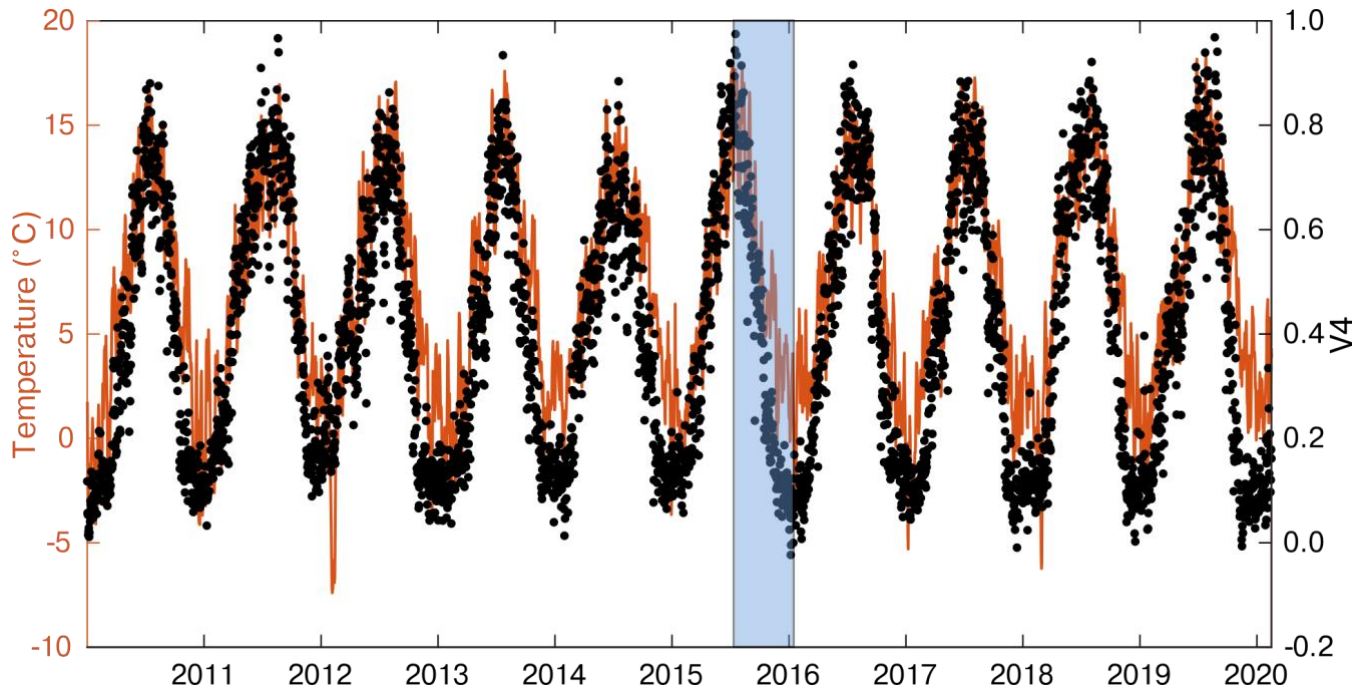
394

395

396

397

Concerning IC4 of the GNSS decomposition, it describes vertical motions in phase, and very well correlated, with the daily mean temperature of the investigated area (Fig. 9). Temperature data are provided by the E-OBS dataset from the EU-FP6 project UERRA (<https://www.uerra.eu>; Cornes et al., 2018). From the point of view of the spatial distribution of this component, most of the stations located in the mountain chain subside when the temperature increases, while the remaining stations uplift as the temperature increases. Figure S15 shows some cross sections plotting the maximum vertical displacements associated with IC4 together with topography, showing this peculiar spatial pattern.



398  
 399 **Figure 9: Comparison between the daily mean temperature of the study area (orange) and the temporal evolution of IC4 (black**  
 400 **dots). The shaded area represents the time interval associated with the maximum displacements shown in Fig. S15.**

### 401 4.3 Vertical ground motion rates and noise analysis

402 We show the impact of the filtering on GNSS displacement rates and uncertainties, where the filtered time-series are the result  
 403 of subtracting from the IGB14-time series the combined displacement associated with the first 4 ICs discussed in Sect. 4.1,  
 404 which represent the combined effect of the seasonal processes in phase with temperature and of the atmospheric and  
 405 hydrological loading. We refer to these corrected time series as ICs filtered time series.

406 Velocities and uncertainties are estimated using the Hector software (Bos et al., 2013), assuming a priori noise models. Noise  
 407 is commonly described as a power-law process

$$408 P_x(f) = P_0(f/f_0)^k \quad (2)$$

409 where  $P_x$  is the power spectrum;  $f$  the temporal frequency;  $P_0$  and  $f_0$  are constants;  $k$  is the spectral index and it indicates the  
 410 noise type.

411 If the power spectrum is flat (i.e., all frequencies have the same power), then the errors are statistically uncorrelated from one  
 412 another, the spectral index is zero and the noise is called “white”. Otherwise the noise shows a dependency with the frequency  
 413 content, and it is referred to as “colored”. In GNSS time series it has been typically observed the presence of noise with a  
 414 power spectrum reduced at high frequencies, with the most popular models being a mix of random walk or “red” noise ( $k = -$   
 415  $2$ ) and flicker or “pink” noise ( $k = -1$ ). Red noise is typically associated with station-dependent effects, while pink noise can  
 416 be associated with mismodeling in GNSS satellites orbits, Earth Orientation Parameters (Klos et al., 2018) and spatially-

417 correlated large-scale processes of atmospheric or hydrospheric origin (Bogusz and Klos, 2016). Flicker plus white noise  
418 model is commonly used in the analysis of GNSS time-series (e.g., Ghasemi Khalkhali et al., 2021 and references therein).  
419 In order to select the best noise model for the input time series, we test different combinations of noise models, choosing the  
420 one with the lowest value of the Akaike Information Criterion (AIC) and of the Bayesian Information Criterion (BIC). In  
421 particular we consider:

- 422 - Flicker + white noise;
- 423 - A general power-law ( $k$  not assigned) + white noise (PL+WN);
- 424 - Flicker + Random walk + white noise.

425

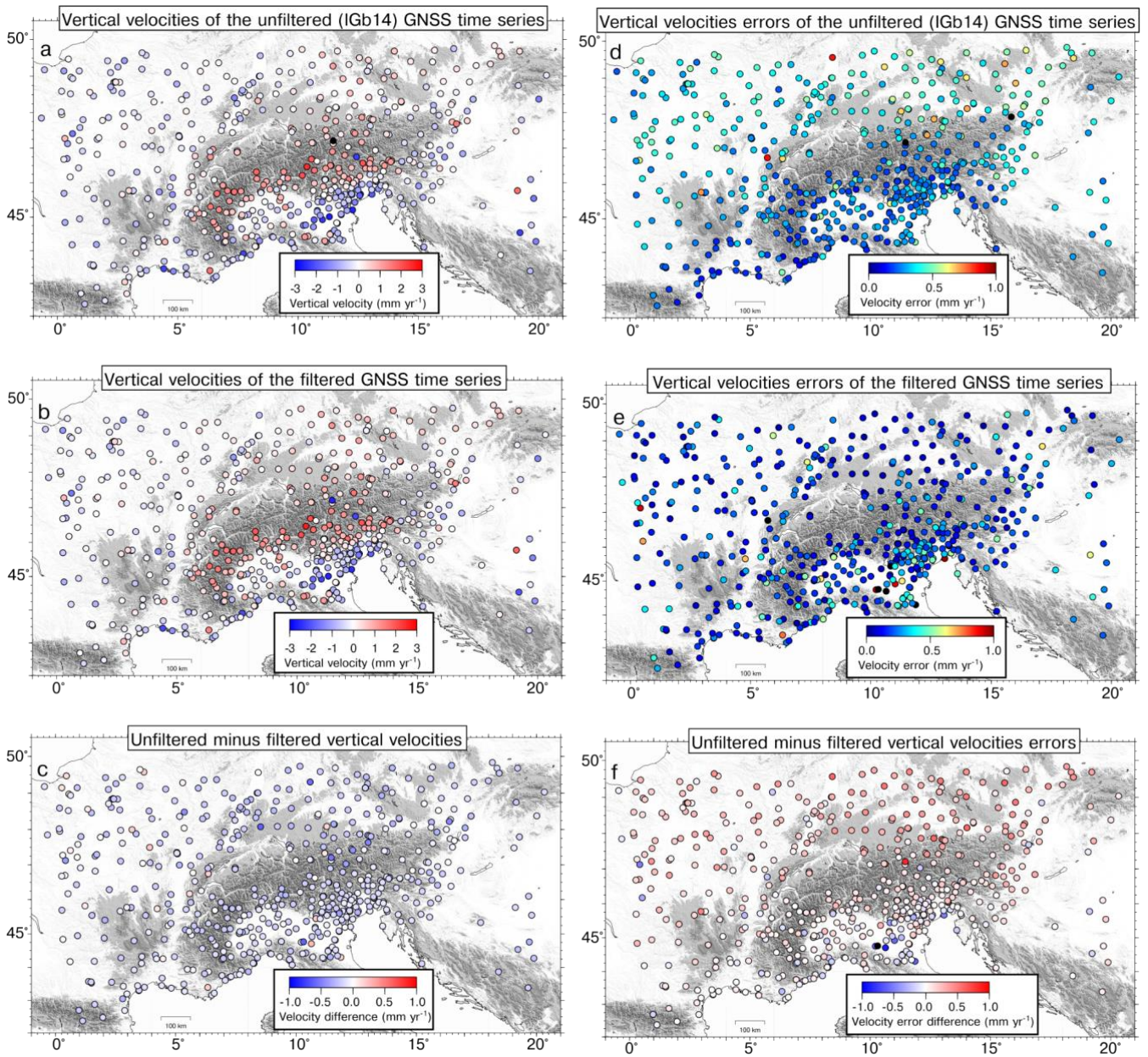
426 Following the AIC and BIC criteria, the preferred noise model is PL+WN, where the parameters of the noise model (i.e., the  
427 spectral index  $k$ ) are estimated by the software using the Maximum Likelihood Estimation (MLE) method. MLE is also used  
428 to estimate the station's rates and the associated uncertainties.

429 We then compare the vertical velocities, and their uncertainties, obtained before and after ICs filtering (Fig. 10). Although  
430 annual and semi-annual signals are often included in the time series modeling, the displacements associated with the first four  
431 ICs already contain these seasonal terms (Fig. 3). Consequently, the ICs filtered time series are modeled only with the linear  
432 trend plus temporal correlated noise, while in the unfiltered time series modeling annual and semi-annual terms are also  
433 included.

434 Fig. 11a shows histograms representing the differences in the vertical velocity estimates obtained from filtered and unfiltered  
435 time-series. The differences are spatially quite homogeneous and of the order of tenths of  $\text{mm yr}^{-1}$ , with a median value of -  
436  $0.15 \text{ mm yr}^{-1}$ . The velocity differences are almost entirely caused by the displacements associated with IC1, which have a  
437 median rate of  $-0.12 \text{ mm yr}^{-1}$ .

438 Concerning the uncertainties associated with the vertical velocity, the impact from ICs filtering is much more important (Fig.  
439 10, f and Fig. S17): the initial median error is  $0.30 \text{ mm yr}^{-1}$ , the final  $0.17 \text{ mm yr}^{-1}$ .

440



441

442

**Figure 10:** a) Vertical velocities from the unfiltered GNSS time-series; b) vertical velocities from ICs filtered time series, obtained after subtracting the displacements associated with the first four ICs; c) difference between the velocities of panel a) minus velocities of panel b). d), e), f), same as a), b), c), but showing the error associated with the vertical velocities.

443

444

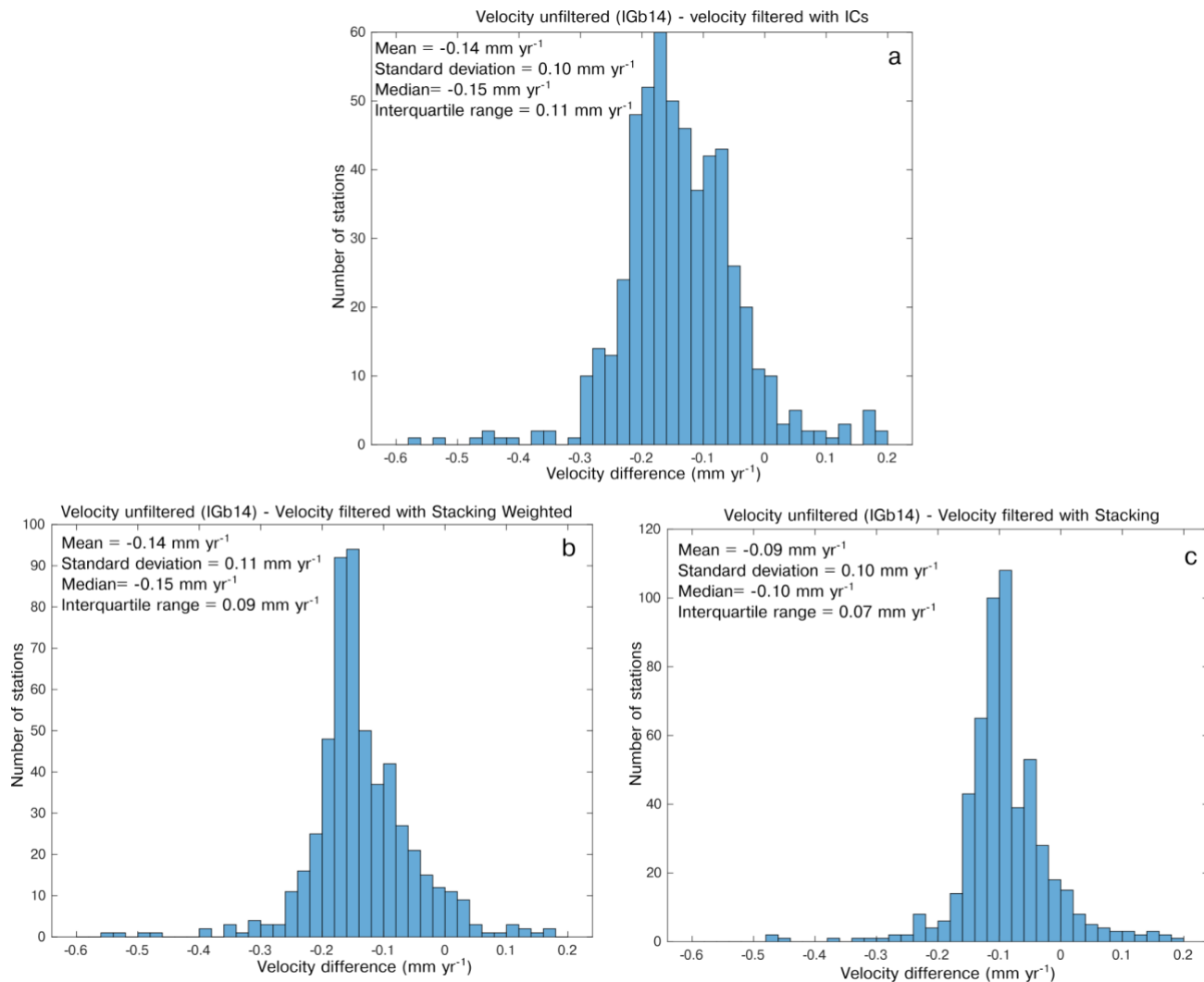
445

446

447

448

449  
450  
451  
452

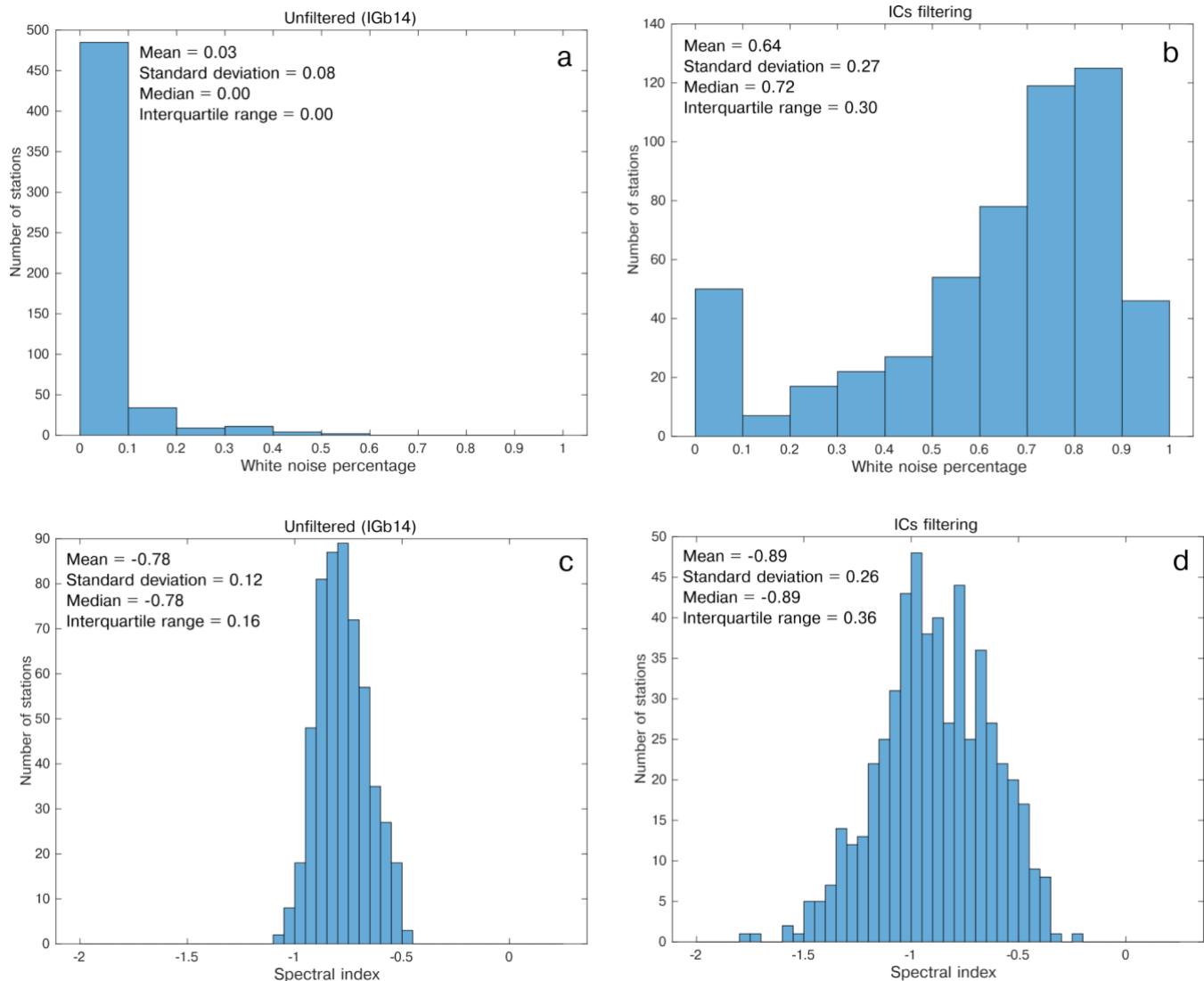


453  
454  
455  
456

**Figure 11: Histogram of the difference between the velocity of the unfiltered time-series and the filtered ones using: a) the displacements associated with the first 4 ICs; b) the Weighted Stacking Filtering Method; c) the Stacking Filtering Method.**

457 The ICs filtering also has a strong impact on the noise characteristics. In fact, while in the unfiltered time series the percentage  
458 of white noise of the PL+WN model is negligible in most of the stations, it becomes dominant in the filtered ones (Fig. 12).  
459 This indicates that a large portion of the power-law noise is associated with the displacements described by the first 4 ICs, i.e.  
460 the atmospheric and hydrological loading and temperature-related processes.





461  
 462 **Figure 12: Histograms of: (a) white noise percentage in the unfiltered time-series and (b) filtered time-series. (c), (d) same as (a) and**  
 463 **(b) for the spectral index. The filtering is done by subtracting the displacements associated with the first 4 ICs.**

464 **5 Discussion**

465 **5.1 Displacement time series filtering**

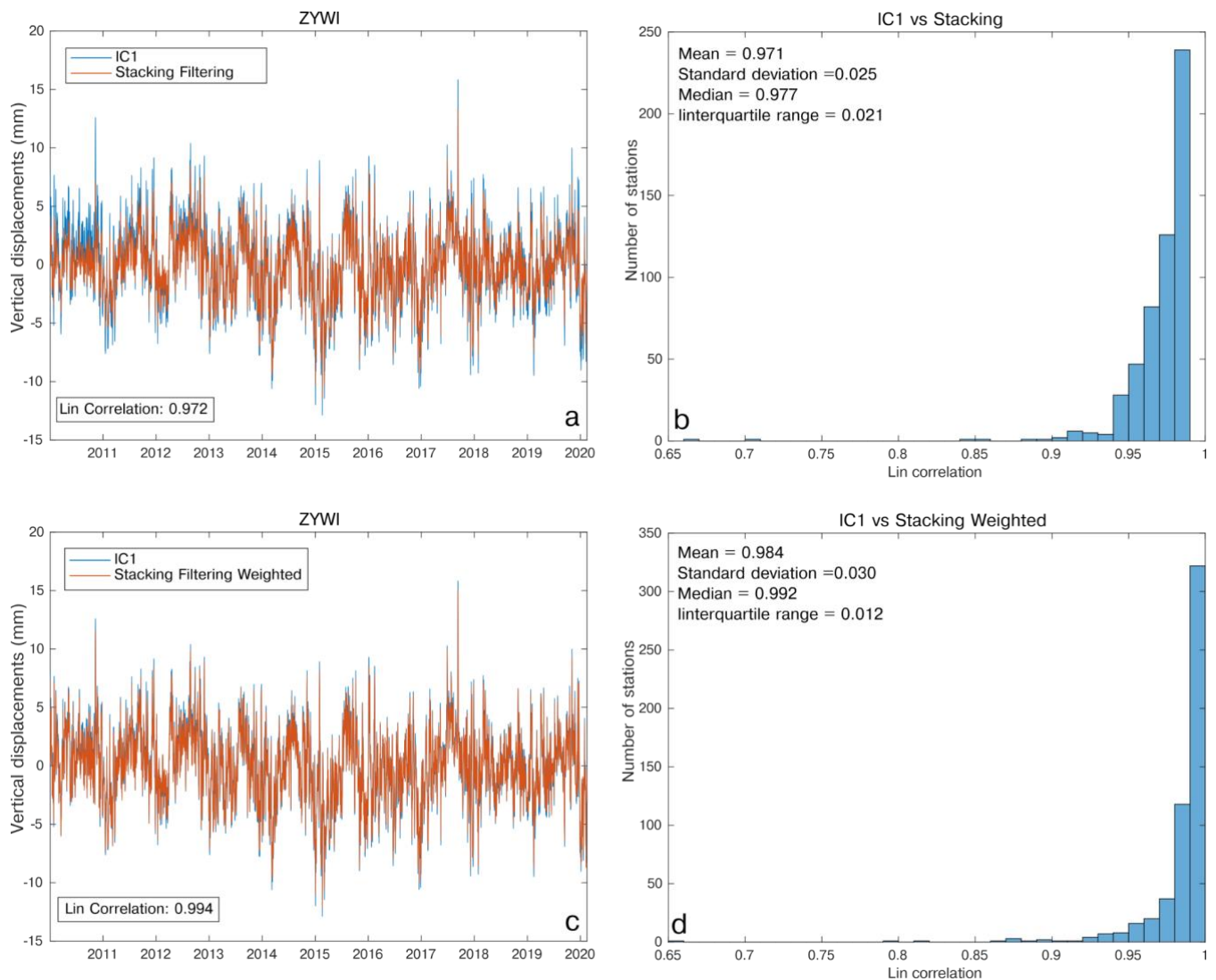
466 Our goal is to estimate the vertical velocity of the GNSS stations associated with long-term geodynamic and tectonic processes,  
 467 then we seek to remove signals associated with meteo-climatic processes. Instead of subtracting from the IGB14-time series  
 468 the modeled displacements, such as those made available through loading services like GFZ, we prefer to subtract the  
 469 displacements associated with the ICs. This approach minimizes biases due to the mismatch between the actual signal caused

470 by atmospheric and hydrological loading and the modeled ones. Larochelle et al. (2018) reached similar conclusions by  
471 comparing GRACE measurements and the results from ICA decompositions of GNSS displacements, which resulted to be  
472 more accurate in correcting GNSS from seasonal displacements than removing GRACE displacements, which smooth local  
473 effects in the data acquisition and processing. In order to support the approach followed, we estimated the scatter of the GNSS  
474 displacement time series by computing the mean standard deviation of 1) the time series given as input to vbICA (IGb14-time  
475 series), 2) the IGB14-time series minus the combined displacement associated with the first 3 ICs and 3) the IGB14-time series  
476 minus the displacements due to HYDL+NTAL from GFZ models. The resulting standard deviation is 5.32, 4.10 and 4.73,  
477 respectively. This demonstrates that removing the displacement associated with the first three ICs is more effective in reducing  
478 the scatter than removing the HYDL+NTAL contribution. Furthermore, in Fig. S19 we show that the filtering with  
479 HYDL+NTAL results in a smaller increase of the white noise percentage in the time series compared to the ICs filtering.  
480 Considering that the stacking methods are widely used to estimate and remove CMS and CME from GNSS time-series (see  
481 Sect. 2), we compare the results obtained adopting the SFM and WSFM methods with the output of vbICA, in particular with  
482 the displacements associated with IC1 (Fig. 3a), which is clearly a CMS, given its homogeneity in its spatial response. CMS  
483 with the stacking methods is estimated using the GNSS\_TS\_NRS code (He et al., 2020) and it is compared with the  
484 displacements associated with IC1 estimating the Lin correlation coefficient. Figure 13 shows that there is an almost-perfect  
485 agreement between the IC1-related displacements and the CMS extracted with both stacking methods, suggesting that even  
486 simple approaches, such as SFM and WSFM, perform well at the scale of the study area.

487 We also estimate the vertical velocities of the GNSS stations after filtering the CMS using the two stacking methods. The rate  
488 differences between unfiltered and filtered time series have a median value of  $-0.15$  and  $-0.10$   $\text{mm yr}^{-1}$ , using the WSFM and  
489 SFM, respectively (Fig. 11b, c). These values are close to the rates associated with IC1 displacements (median =  $-0.12$   $\text{mm yr}^{-1}$ ),  
490 which are the primary cause of the velocity difference obtained from IGB14 and ICs filtered time-series, suggesting that the  
491 rate difference does not strongly depend on the filtering method adopted.

492 As already shown in Sect. 4.3, the errors associated with the velocities of the unfiltered and filtered time series, which have  
493 median values of  $0.30$  and  $0.17$   $\text{mm yr}^{-1}$ , respectively, have about the same value of the velocity difference between filtered  
494 and unfiltered time series. It follows that the velocity differences are, from a statistical point of view, barely significant.

495 Nonetheless, it is worth considering that, according to the LSDM-based model, the displacements resulting from the combined  
496 effect of hydrological and atmospheric loading have a negative rate (median =  $-0.11$   $\text{mm yr}^{-1}$ ; Fig. S16c) in agreement with  
497 the rate observed for IC1 (V1 in Fig. 3), suggesting that environmental loading may cause a small subsidence, at least in the  
498 observed time-span, which is captured by IC1. However, the rates of the displacements due to hydrological loading are model-  
499 dependent: according to LSDM, they show a negative linear trend (Fig. S16b), as opposed to what is observed using the EOST  
500 model (Fig. S16e). As a result, the rates of the displacements due to atmospheric + hydrological loading computed using the  
501 EOST model are not in agreement with the rates of the IC1 displacements. This is most likely a consequence of the differences  
502 in modeling the hydrological loading-induced displacements; in particular, the EOST model takes into account only water  
503 stored as snow and soil moisture, whereas the LSDM model also includes the contribution of rivers, lakes and wetlands.



504

505 **Figure 13: Comparison between the displacement associated with IC1 at the ZYWI site and the CME estimated with**  
 506 **the Stacking Filtering Method (a) and the Weighted Stacking Filtering Method (c). We also show the histogram**  
 507 **representing the Lin correlation between the displacements associated with the IC1 and the CME estimated with the**  
 508 **Stacking Filtering Method (b) and the Weighted Stacking Filtering Method (d) at each site. We point out that the CME**  
 509 **computed with the aforementioned methods is, by definition, the same at each station; whereas the displacements**  
 510 **associated with IC1 have the same temporal evolution but (slightly) different amplitudes. We plot the station ZYWI as**  
 511 **an example.**

512

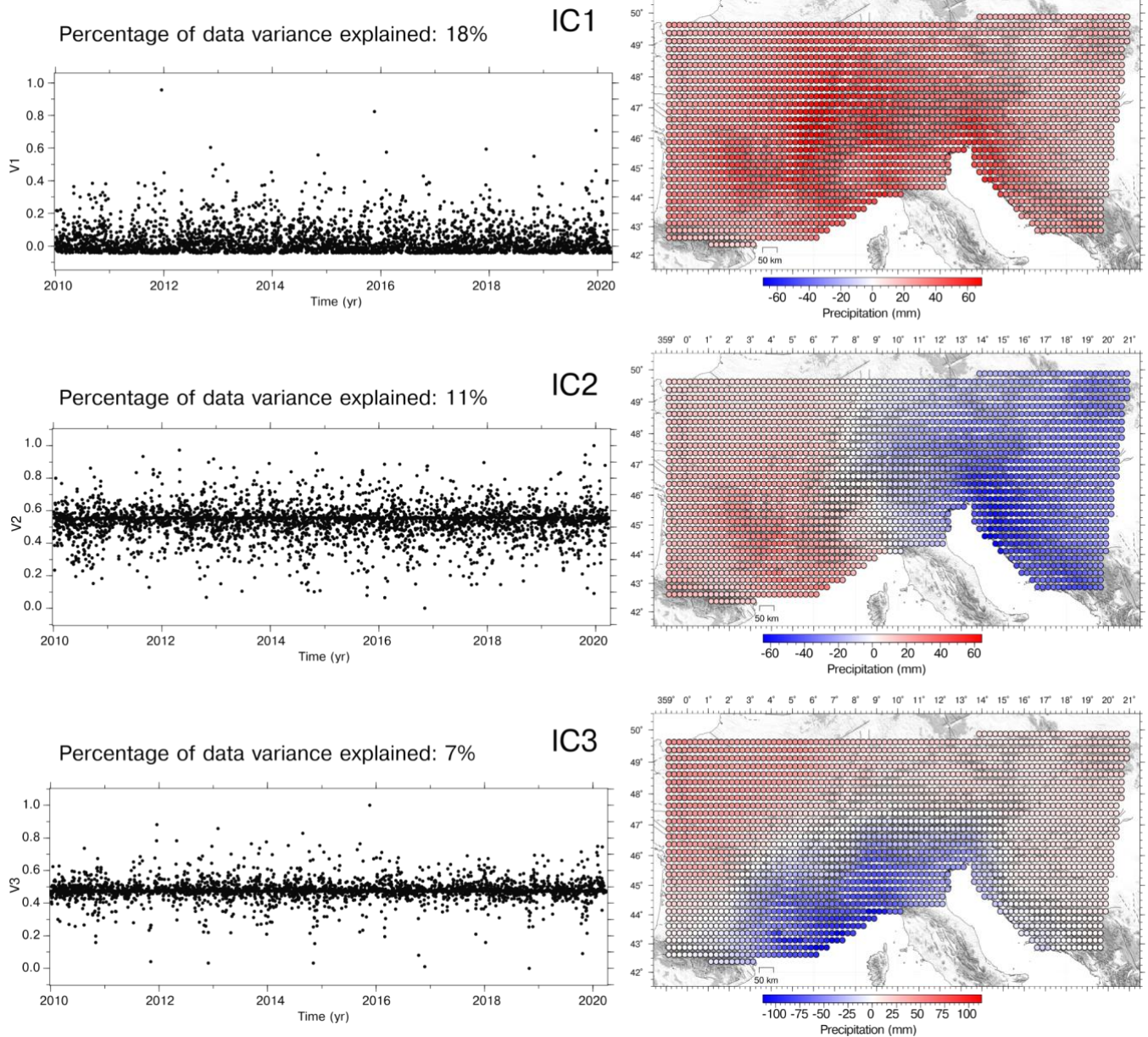
513 The stacking methods used to estimate the CMS are easier and faster to implement than the vbICA analysis. Depending on the  
 514 research target, these common mode signals might be worth removing, in order to obtain a more precise, and eventually

515 accurate, estimation of the GNSS linear velocities or retained to study, for example, seasonal deformation. Multivariate  
516 statistics and/or source separation algorithms applied to ground displacement time-series allow one to extract and interpret  
517 them in terms of the physics behind them, through a comparison with other displacement datasets or models. Furthermore,  
518 time series can be filtered not only from CMS, but also from signals associated with spatially uncorrelated processes, as we  
519 did in Sect. 4.3 estimating the vertical velocities filtered from non-tectonic processes related to the first four ICs.  
520 In Sect. 4.3 we also show that the colored noise in the time series is significantly reduced by the ICs filtering. This result is in  
521 agreement with the results of recent studies conducted in other regions, such as Antarctica (Li et al., 2019) and China (Yuan  
522 et al., 2018). Both studies show that ICA or PCA filtering of GNSS time series suppress the colored noise amplitudes but have  
523 little influence on the amplitude of the white noise. Furthermore, Klos et al. (2021) analyzes the effect of atmospheric loading  
524 on the noise of GNSS stations in the European plate, finding that the noise is whitened when NTAL contribution is removed.  
525 The description of atmospheric processes at the scale of the Alps can be seen as small scale when compared, for example, to  
526 the circulation in the northern hemisphere. Small scale processes are usually interpreted as noise, but they may affect the large-  
527 scale dynamics (e.g., Faranda et al., 2017). It follows that these small scale processes should be represented with an appropriate  
528 stochastic formulation. Since the CMS are typically characterized by PL+WN noise, the link that we find between CMS and  
529 atmospheric and hydrological signals could provide a hint on the type of noise that is more suitable to describe such small  
530 scale perturbations when modeling the large-scale dynamics of the atmosphere.

## 531 **5.2 ICs interpretation**

532 Our analysis supports the interpretation that the displacements associated with IC1, IC2 and IC3 are likely due to the combined  
533 effect of the hydrological and atmospheric loading, whose spatial responses are not homogeneous over the study area. In  
534 support of this interpretation we can refer to Brunetti et al. (2006), who applied a PCA to precipitation data in the great Alpine  
535 area. They highlighted the presence of N-S and E-W gradients in the spatial response of meteo-climating forcing processes.  
536 The authors suggest that the main cause of the spatial and temporal variability of the precipitation is the North Atlantic  
537 Oscillation (NAO), which also causes fluctuation of the atmospheric pressure (Vicente-Serrano and López-Moreno, 2008). It  
538 is then likely that weather regimes like the NAO and the Atlantic Ridge, influence both NTAL and HYDL, which is mainly  
539 forced by precipitation, so that the spatial patterns of the ICs associated with atmospheric and hydrological loading are the  
540 same of NAO (N-S) and Atlantic Ridge (E-W).  
541 The vbICA algorithm is not able to separate NTAL and HYDL because they are not independent from a mathematical point  
542 of view. This emerges also from the recent work by Tan et al. (2022), who performed an ICA on GNSS time series of the  
543 Yunnan Province of China and interpreted IC1 as the average effects of the joint patterns from soil moisture and atmospheric-  
544 induced annual surface deformations. Let us consider for example the case of IC2\_NTAL and IC2\_HYDL. They have two  
545 different temporal evolutions ( $V2\_NTAL$  and  $V2\_HYDL$ ); but the spatial distributions ( $U2\_NTAL$  and  $U2\_HYDL$ ) have the  
546 same pattern, i.e. they only differ for a weighting factor  $k$ . Then, we can write  $U2\_NTAL = k * U2\_HYDL$ .  
547 The displacement  $d$  resulting from the combined effect of IC2\_NTAL and IC2\_HYDL is then:

548  $d = IC2\_NTAL + IC2\_HYDL = U2\_NTAL * V2\_NTAL + U2\_HYDL * V2\_HYDL = U2\_HYDL * (k * V2\_NTAL + V2\_HYDL)$ .  
549 As a result, the displacement due to  $IC2\_NTAL + IC2\_HYDL$  is identified by a single spatial distribution  $U2\_HYDL$  and a  
550 temporal evolution  $k * V2\_NTAL + V2\_HYDL$ . Then, if we do not make any prior assumptions about  $V2\_NTAL$  and  
551  $V2\_HYDL$ , it is not possible to separate  $IC2\_NTAL$  and  $IC2\_HYDL$  from a statistical point of view.  
552 In Sect. 4.2 we show that not only  $IC2\_NTAL$  and  $IC2\_HYDL$  have very similar spatial patterns, but also  $IC1\_NTAL$  and  
553  $IC1\_HYDL$ ,  $IC3\_NTAL$  and  $IC3\_HYDL$  have similar spatial responses. Then, the GNSS time-series decomposition in the  
554 Alpine area does not allow separating the effect of the hydrological loading from the atmospheric loading with an ICA  
555 approach.  
556 We also performed a vbICA analysis on precipitation data (RAIN) recorded over the study region, using 3 ICs (Fig. 14). The  
557 spatial pattern of the ICs is analogous to the ones associated with  $NTAL$  and  $HYDL$  (Fig. 4 and Fig. 5).  
558

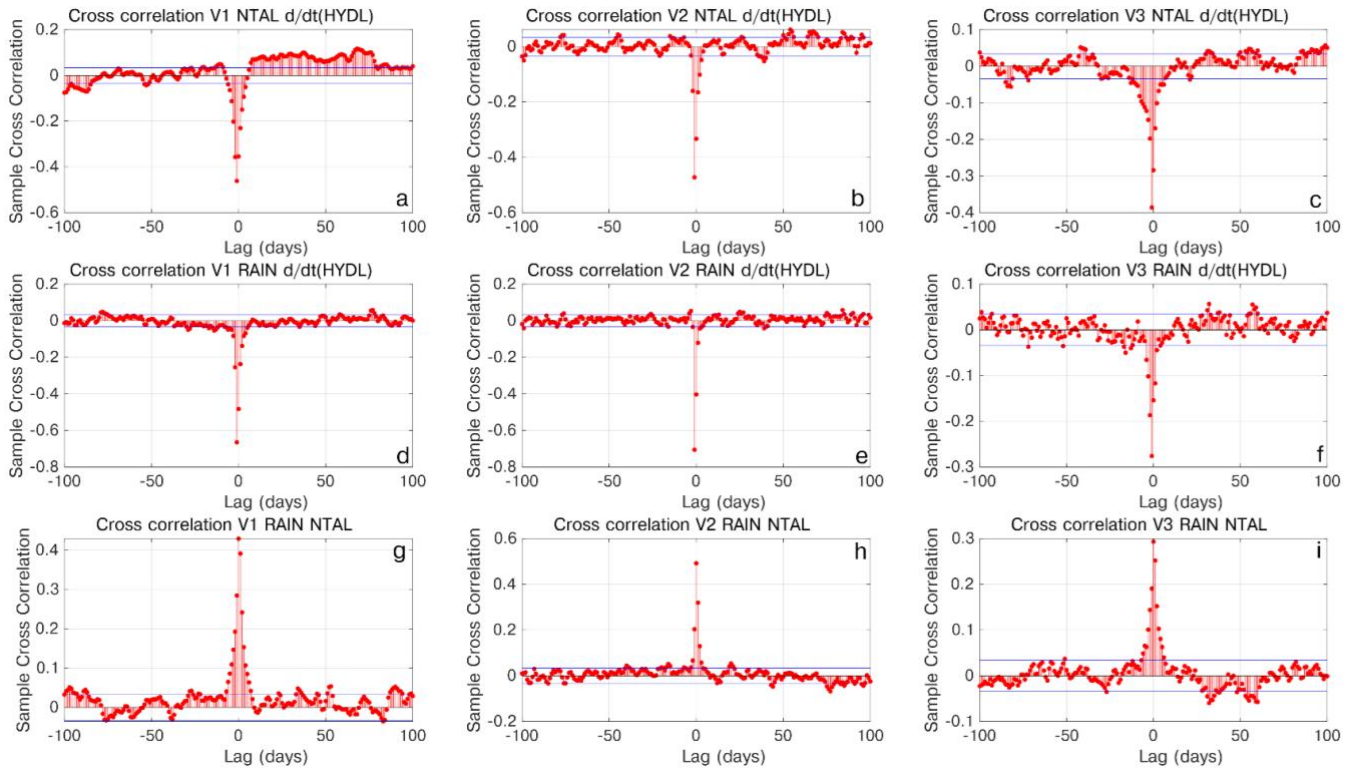


559  
 560 **Figure 14: IC1, IC2 and IC3 of the RAIN decomposition.**  
 561

562 This supports the hypothesis that precipitation, atmospheric pressure, hydrological loading and ground displacement are  
 563 somehow interconnected and characterized by a common climate-related forcing, whose characteristics of spatial variability  
 564 are described by the NAO and Atlantic Ridge weather regimes.

565 We point out that HYDL, NTAL and GNSS are models or measurements of vertical displacements, which are positive when  
 566 upward and negative when downward; while RAIN is the amount of fallen rain per unit area.

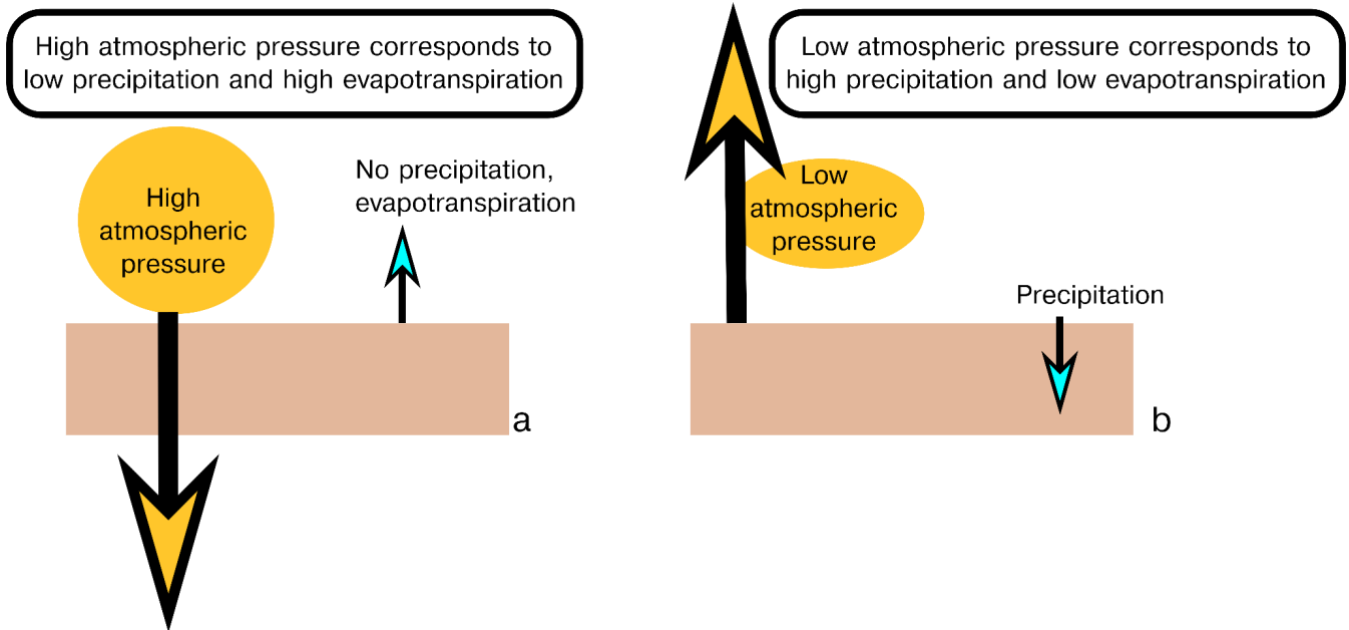
567 Let us consider for the sake of simplicity the IC1 case, but what we are going to discuss holds true also for IC2 and IC3.  
 568 The temporal evolution of NTAL\_IC1 (NTAL\_V1) is correlated with the temporal evolution of RAIN\_IC1 (RAIN\_V1, Fig.  
 569 15g-i) and anti-correlated with the time derivative of the temporal evolution of HYDL\_IC1 (HYDL\_V1, Fig. 15a-c).  
 570 HYDL\_V1 is also highly anti-correlated with RAIN\_IC1 (Fig. 15d-f).



571 **Figure 15: Cross correlation between:**  
 572 **a) the temporal evolution of the IC1 of the NTAL decomposition and the time derivative of the temporal evolution of the IC1 obtained**  
 573 **by decomposing HYDL; b) same as a), but considering IC2; c) same as a), but considering IC3;**  
 574 **d) the temporal evolution of the IC1 of the precipitation data decomposition and the time derivative of the temporal evolution of the**  
 575 **IC1 obtained by decomposing HYDL; e) same as d), but considering IC2; f) same as d), but considering IC3;**  
 576 **g) the temporal evolution of the IC1 of the NTAL decomposition and the temporal evolution of the IC1 of the precipitation data**  
 577 **decomposition; h) same as g), but considering IC2; i) same as g), but considering IC3.**

580 Our interpretation of the correlations discussed above, schematically represented in Fig. 16, is the following: when the weather  
 581 goes from a low pressure to a high pressure regime, the increasing pressure causes a downward displacement of the ground  
 582 (Fig. S8). Anyway, low pressure regimes are often associated with precipitation, and that is why IC1\_RAIN and IC1\_NTAL  
 583 are correlated. It follows that when we go from high pressure to low pressure conditions, the ground motion, if we assume a  
 584 pure elastic process, is affected by two forces acting in opposite directions: the decreasing atmospheric pressure induces uplift,

585 while the precipitation load causes downward motion. Rain also affects hydrological loading, increasing it and causing a  
586 downward ground motion. As a consequence, the temporal derivative of HYDL\_IC1, which is more sensitive to small but fast  
587 variation of hydrological loading than HYDL itself, is negative and anti-correlated with IC1\_RAIN.  
588



589 **Figure 16: Schematic representation of the ground vertical displacement due to elastic deformation during high pressure (a) and**  
590 **low pressure (b) conditions. Yellow arrows reflect displacements associated with atmospheric pressure, blue arrows reflect**  
591 **displacements associated with precipitation and evapotranspiration.**  
592

593  
594 Atmospheric pressure variations happen at fast temporal scales, then the switch from high to low pressure conditions (and vice  
595 versa) can happen in a few days and cause quite large (centimetric) ground vertical displacements. Hydrological loading acts  
596 at longer timescales and there are several factors to consider besides precipitation, in particular the temperature, which causes  
597 evapotranspiration. Nonetheless, computing the time derivative of the hydrological loading allows to detect “fast” variations  
598 due to the change of the atmospheric pressure and the precipitation events often associated with it.

599 The interpretation of IC4 is less straightforward and the pattern we see in the Alps (Figure S.15) is not easy to explain. Air  
600 temperature increase can induce both positive and negative vertical displacements. One possible mechanism to explain  
601 negative vertical displacements associated with temperature increase is that in the alpine valleys the water content increases  
602 as the temperature increases because of the snow and ice melting. It follows that in those areas the elastic response to  
603 hydrological load is higher during summertime than winter, as observed by Capodaglio et al. (2017), so that negative vertical  
604 displacements are measured when the temperature increases. Then, it is not surprising that in the alpine valleys the stations  
605 affected by large IC4-related displacements move downward as temperature increases. This may be an example of a small-



606 scale hydrological process that is likely badly reproduced by the HYDL displacement dataset, which does not have a spatial  
607 resolution fine enough to represent hydrological loading displacements at the scale of the alpine valleys. Other site-dependent  
608 processes that can potentially induce uplift during winter are the ice formation, and subsequent melting, in the antenna and  
609 antenna mount (Koulali and Clarke, 2020) and soil freezing (Beck et al., 2015).

610 Conversely, positive vertical displacements as the temperature increases can be caused by monument/bedrock thermal  
611 expansion and the drying of the soil, because of the reduction of the hydrological load. While HYDL takes into account the  
612 drying of the soil, we cannot exclude that some local, unmodeled, environmental conditions can amplify this effect at some  
613 sites. This might explain why most of the sites affected by uplift during temperature increases are located in plain areas, like  
614 the northern sector of the Paris Basin and in the Po plain, instead of the mountainous ones.  
615 The relation between IC4 and local processes is also suggested by the heterogeneity of this signal in terms of its spatial  
616 distribution, sign, amplitude and relevance in explaining the data variance. In fact, while ~50% of the stations have  $U_4 < 2\text{mm}$   
617 (Fig. S3d) and explain  $< 1\%$  of the data variance, meaning that IC4 is almost useless to reproduce the original data, there is a  
618 non-negligible number of stations (~10%) explaining  $> 10\%$  of the data variance and with  $U_4 > 6\text{mm}$ . Finally, possible sources  
619 of this seasonal signal might be systematic errors in GNSS observations and in their modeling (Chanard et al., 2020).  
620 In the introduction we mentioned the effects of the non-tidal ocean loading on the vertical displacements and both LSDM-  
621 based and EOST models provide estimation of them. In the study region, this process induces displacements that are  
622 significantly smaller than both atmospheric and hydrological loading, due to the distance from the oceans of the study area, so  
623 we do not take it into account. According to the estimation of the LSDM-based model, the maximum amplitude of the spatial  
624 mean over the study region of the displacements associated with it is 4.3 mm; while the maximum amplitude of the  
625 displacements associated with atmospheric and hydrological loading are 23.8 mm and 12.2 mm, respectively. Figure S5  
626 provides a comparison of the spatial mean of the displacements associated with the three deformation mechanisms.

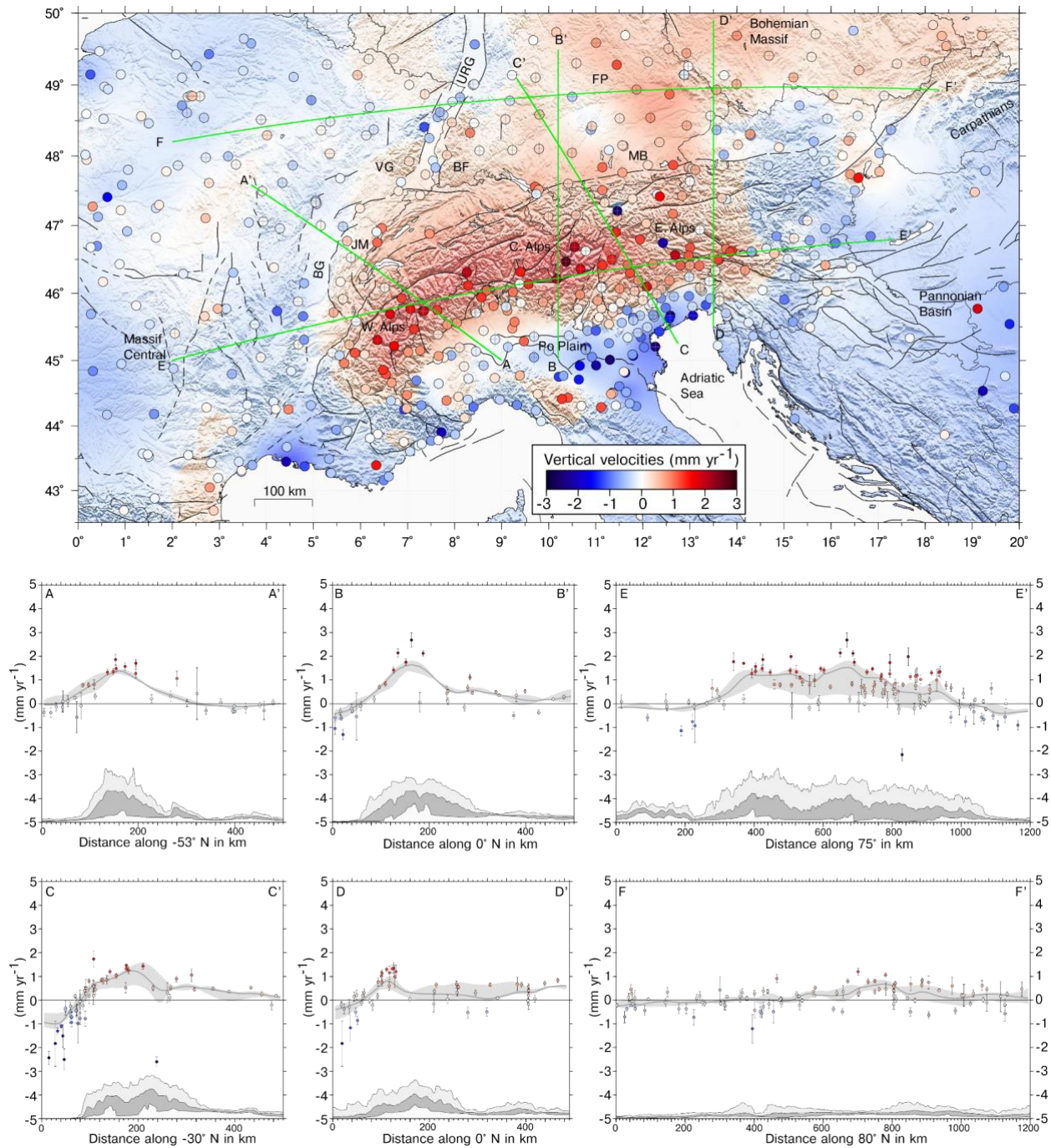
### 627 **5.3 Vertical velocity gradients across the Alps**

628 The vertical velocity field of the IGB14-time series and of the IGB14-time series with the contribution of the first 4 ICs removed  
629 (ICs filtered) do not differ much in terms of uplift/subsidence patterns (see Fig. 11), both showing the belt of continuous uplift,  
630 of the order of  $1\text{-}2\text{ mm yr}^{-1}$ , along the Alpine mountain chain. As shown in Fig. 11c, the vertical velocities from filtered time-  
631 series show barely faster positive rates, mainly as an effect of filtering out hydrological and atmospheric displacements of IC1,  
632 as discussed above. Figure 17 shows the continuous vertical velocity field obtained from the discrete values adopting the  
633 multiscale, wavelet-based, approach described in Tape et al. (2009), and some vertical velocity and topographic profiles  
634 running across the great Alpine area. The same figure obtained using velocities and uncertainties from unfiltered time-series  
635 is shown in the Supplementary Information (Fig. S20). Despite the similarity in the velocity patterns, the improvements in  
636 both the precision and consistencies of vertical spatial gradients are apparent in cross section view. Profile E-E' in Fig. 17  
637 shows positive vertical rates increasing from W to E, with the maximum uplift rates in the central Alps, and the positive  
638 correlation with the topography along the chain axis, with decreasing rates toward the east, changing to subsidence east of

639 Lon.  $\sim 14.5^\circ$  E, while entering the Pannonian basin domain. The correlation with topography is also clear in the chain-normal  
640 profiles (A-A', B-B', C-C' and D-D'). In the Western and Central Alps (A-A' and B-B') the maximum uplift rates are located  
641 in correspondence with the maximum elevation, whereas in the Eastern Alps (C-C' and D-D') the maximum uplift rates are  
642 shifted southward. The Eastern Southern Alps is the region where the largest part of the Adria-Eurasia converge is  
643 accommodated ( $1-3 \text{ mm yr}^{-1}$ ), through active thrust faults and shortening (Serpelloni et al., 2016). Here, maximum uplift rates  
644 are likely due to interseismic deformation, and their position, across the belt, is driven by thrust fault geometries, slip-rates and  
645 locking depths (Anderlini et al., 2020). Concerning the south Alpine foreland in the Po Plain and Venetian plain, Fig. 17 shows  
646 a decrease in the vertical velocities from west to east, with barely positive rates in the western Po Plain and increasing  
647 subsidence rates in the northern Adriatic and in the northern Apennines foreland.

648 In the Alpine foreland, positive, sub- $\text{mm yr}^{-1}$ , velocities are present in the Jura Mts. and the Molasse basin, but uplift extends  
649 further northward in the Black Forest and the Franconian Platform, in southern Germany, and in the southern part of the  
650 Bohemian Massif. Overall, in the portion of central Europe investigated in this work, we see two different patterns: prevalent  
651 stable to slowly-subsiding sites ( $< 1 \text{ mm yr}^{-1}$ ) are present west of the Rhine graben, whereas a prevalence of slowly uplifting  
652 sites ( $< 1 \text{ mm yr}^{-1}$ ) is present east of it. Profile F-F' in Fig. 17 better highlights this pattern. Across the Upper Rhine Graben,  
653 the weak uplift signal in the graben's shoulders, the Vosges Mts and Black Forest, is associated with subsidence of stations  
654 located within the graben, according to Henrion et al. (2020). To the east, uplift in the Franconian Platform and the Bohemian  
655 Massif is only partially correlated with topography. It is still debated whether uplifted regions across NW Europe attest to  
656 lithospheric buckling in front of the Alpine arc or were randomly produced by a swarm of baby plumes. Uplift propagation by  
657 interferences with the Western Carpathians and possible mantle processes, as suggested by the positive dynamic and residual  
658 topography (Faccenna et al., 2014), may contribute to the observed uplift in the Bohemian Massif.

659 Sternai et al. (2019) investigated the possible relative contribution of different geophysical and geological processes in the  
660 actual vertical velocity budget over the Alps, suggesting that the interaction among tectonic and surface mass redistribution  
661 processes, rather than an individual forcing, better explain vertical deformation in the Alps. Mey et al. (2016) suggested that  
662  $\sim 90\%$  of the present-day uplift of the Alpine belt is due to the melting of the LGM ice cap. While it is difficult to independently  
663 constrain the patterns and magnitude of mantle contributions to ongoing Alpine vertical displacements at present, lithospheric  
664 adjustment to deglaciation and erosion are by far the most important ongoing process, but other authors suggest that other  
665 processes are currently shaping the vertical ground motion pattern. In the western and central Alps, active convergence is  
666 inactive or limited, the residual uplift rates, after correction from isostatic contributions, are likely due to deep-seated mantle  
667 processes, including for example detachment of the western European slab and dynamic contributions related to sub-  
668 lithospheric mantle flow (Chery et al., 2016; Nocquet et al., 2016; Sternai et al., 2019). A tectonic contribution to the ongoing  
669 uplift is, instead, more likely in the Eastern Alps, and in particular in the Southeastern Alps, where the Adria-Europe  
670 convergence is accommodated. However, Anderlini et al (2020) observed that more accurate glacio isostatic models would be  
671 needed when interpreting tectonic contributions to uplift at the edge of ice caps, as in the Eastern Southern Alps.



672

673

674

675

**Figure 17: Vertical velocities from filtered time-series (colored circles), continuous velocity field, topographic and swath profiles across the great Alpine area. Each profile (green line) encompasses a 50+50 km swath. BG: Bresse Graben; JM: Jura Mts.; VG: Vosges Mts.; BF: Black Forest; URG: Upper Rhine Graben; FP: Franconian Platform; MB: Molasse Basin.**

## 676 **6 Conclusions**

677 The application of a blind source separation algorithm to vertical displacement time-series obtained from a network of GNSS  
678 stations in the Great Alpine Area allows us to identify the main sources of vertical ground deformation. Besides the linear  
679 trend, vertical displacements are influenced by: 1) atmospheric pressure loading, 2) hydrological loading and 3) seasonal  
680 processes in phase with temperature. The analysis of displacement time series of environmental loading shows that the largest  
681 vertical motions are related to the variation of atmospheric pressure, in particular when considering daily/weekly timescales.  
682 Seasonal displacements are more clearly associated with hydrological loading and processes in phase with temperature.  
683 However, while deformation associated with temperature is well isolated, we were not able to clearly separate the atmospheric  
684 and hydrological loading signals in the GNSS displacement time-series.

685 We use the results of the time-series decomposition to filter the IGB14 time-series and study the effect of removing signals  
686 associated with environmental loading and temperature-related processes on the vertical velocities and uncertainties.  
687 Removing these signals causes a quite uniform, but limited ( $\sim 0.1 \text{ mm yr}^{-1}$ ), increase of the velocities, which we interpret as  
688 due to the small negative linear trend associated with the atmospheric and hydrological loading-induced displacements. It is  
689 worth noting that the procedure used in this work to estimate the station velocities does not allow to distinguish the tectonic  
690 velocities from the contribution to the velocity induced by climate-related processes, in particular if the linear trend associated  
691 with ATML and/or HYDL time series is large. Furthermore, the filtering almost halves the uncertainties associated with the  
692 velocities and changes the noise spectra, increasing the white noise percentage to the detriment of the colored one.

693 Although providing a geological/geophysical explanation for the observed vertical velocity pattern is out of the scope of this  
694 work, we can conclude that more precise and accurate vertical velocities, such as the one presented in this work, can be obtained  
695 by careful signal detection and filtering. This can help develop better spatially resolved models, aiming at a more effective  
696 understanding of the relative contribution of the different ongoing geodynamic and tectonic processes shaping the present-day  
697 topography of the Alps.

## 698 **Code and data availability**

699 The MATLAB code for vbICA decomposition is available from <http://dx.doi.org/10.17632/n92vwbg8zt.1>. Global datasets  
700 used for the hydrological, atmospheric and ocean load model are taken from <http://loading.u-strasbg.fr/> (EOST model) and  
701 <http://rz-vm115.gfz-potsdam.de:8080/repository/entry/show?entryid=24aacdfef9b0-43b7-b4c4-bdbe51b6671b> (LSDM-  
702 based model). Precipitation data are available on [https://disc.gsfc.nasa.gov/datasets/GPM\\_3IMERGDF\\_06/summary](https://disc.gsfc.nasa.gov/datasets/GPM_3IMERGDF_06/summary).  
703 Temperature data are available on <https://www.ecad.eu/download/ensembles/download.php> and IGB14 GPS time series on  
704 <https://doi.pangaea.de/10.1594/PANGAEA.938422>.

705 **Author contribution**

706 F. Pintori conceived and led the paper, E. Serpelloni coordinated the study and analyzed GNSS data, A. Gualandi supervised  
707 the vbICA analysis of GNSS displacements. All the authors discussed the content of the paper and shared the writing.

708 **Competing interests**

709 The authors declare that they have no conflict of interest.

710 **Acknowledgements**

711 We thank E. Scoccimarro and M. Zampieri for fruitful suggestions on the interpretation of meteo-climatic data. F. Pintori was  
712 supported by the project TRANSIENTI, founded by the Italian Ministry of Education, Universities and Research (MIUR)  
713 “Premiale 2014”. Adriano Gualandi is supported by European Research Council Advance Grant 835012 (TECTONIC). This  
714 work has been developed in the framework of the project KINDLE, funded by the “Pianeta Dinamico” INGV institutional  
715 project. We acknowledge the E-OBS dataset from the EU-FP6 project UERRA (<https://www.uerra.eu>) and the Copernicus  
716 Climate Change Service, and the data providers in the ECA&D project (<https://www.ecad.eu>). We are grateful to the many  
717 agencies, companies and networks that have made GNSS data available. We specifically thank the following public networks  
718 and institutions for raw RINEX data: IGS, EUREF-EPN, AGROS (Serbia), CZEPOS (Czech Republic), GPS-EMILIA  
719 ROMAGNA (Italy), InOGS-FREDNET (Italy), Rete GNSS Marussi FVG (Italy), ASI-GEODAF (Italy), GEONAS (Czech  
720 Republic), GFZ (Germany), GREF (Germany), Leica-Geosystem HXGN-SmartNeT (Italy), GNSS LIGURIA (Italy), Topcon  
721 Positioning Italy NETGEO (Italy), OLGGPS (Austria), RENAG (France), RGP (France), INGV-RING (Italy), SIGNAL  
722 (Slovenia), SONEL, SPINGNSS (Italy), STPOS (BZ, Italy), TPOS (TN, Italy), GPS-VENETO (Italy), VESOG (Czech  
723 Republic). ORPHEON data were provided to the authors for scientific use in the framework of the GEODATA-INSU-CNRS  
724 convention. We acknowledge Echtzeit Positionierung Austria for providing access to the EPOSA data. SAPOS networks are  
725 operated by various German States (Landesamt für Digitalisierung, Breitband und Vermessung and Baden-Württemberg).

726 **References**

727 Anderlini, L., Serpelloni, E., Tolomei, C., De Martini, P. M., Pezzo, G., Gualandi, A. and Spada, G.: New insights into active  
728 tectonics and seismogenic potential of the Italian Southern Alps from vertical geodetic velocities, , [https://doi.org/10.5194/se-](https://doi.org/10.5194/se-2020-10)  
729 2020-10, 2020.

730 Beck, I., Ludwig, R., Bernier, M., Strozzi, T. and Boike, J.: Vertical movements of frost mounds in subarctic permafrost  
731 regions analyzed using geodetic survey and satellite interferometry, *Earth Surf. Dynam.*, 3(3), 409–421,  
732 <https://doi.org/10.5194/esurf-3-409-2015>, 2015.

733 Bevis, M. and Brown, A.: Trajectory models and reference frames for crustal motion geodesy, *J. Geod.*, 88(3), 283–311,  
734 <https://doi.org/10.1007/s00190-013-0685-5>, 2014.

735 Blewitt, G., Hammond, W. and Kreemer, C.: Harnessing the GPS data explosion for interdisciplinary science, *EOS*, 99,  
736 <https://doi.org/10.1029/2018EO104623>, 2018.

737 Bogusz, J. and Klos, A.: On the significance of periodic signals in noise analysis of GPS station coordinates time series, *GPS*  
738 *Solut.*, 20(4), 655–664, <https://doi.org/10.1007/s10291-015-0478-9>, 2016.

739 Bos, M. S., Fernandes, R. M. S., Williams, S. D. P. and Bastos, L.: Fast error analysis of continuous GNSS observations with  
740 missing data, *J. Geod.*, 87(4), 351–360, <https://doi.org/10.1007/s00190-012-0605-0>, 2013.

741 Brunetti, M., Maugeri, M., Nanni, T., Auer, I., Böhm, R. and Schöner, W.: Precipitation variability and changes in the greater  
742 Alpine region over the 1800–2003 period, *J. Geophys. Res.*, 111(D11), <https://doi.org/10.1029/2005JD006674>, 2006.

743 Capodaglio, P., Naldi, M. and Simonetto, F.: Hydrogeological characterization throughout deep geophysical investigations in  
744 the Verrès plain (Aosta Valley, north-western Italian Alps), *Acque Sott.*, 6(1), <https://doi.org/10.7343/as-2017-262>, 2017.

745 Chanard, K., Métois, M., Rebischung, P. and Avouac, J.P: A warning against over-interpretation of seasonal signals measured  
746 by the Global Navigation Satellite System. *Nat. Commun. Mar* 13;11(1):1375. <https://doi.org/10.1038/s41467-020-15100-7>,  
747 2020

748 Chery, J., Genti, M. and Vernant, P.: Ice cap melting and low-viscosity crustal root explain the narrow geodetic uplift of the  
749 Western Alps, *Geophys. Res. Lett.* 43 (7), 3193–3200, <https://dx.doi.org/10.1002/2016GL067821>, 2016.

750 Ching, K.-E., Hsieh, M.-L., Johnson, K. M., Chen, K.-H., Rau, R.-J., and Yang, M.: Modern vertical deformation rates and  
751 mountain building in Taiwan from precise leveling and continuous GPS observations, 2000–2008. *Journal of Geophysical*  
752 *Research*, 116, B08406, <https://doi.org/10.1029/2011JB008242>, 2011.

753 Choudrey, R. A.: Variational Methods for Bayesian Independent Component Analysis. Pattern analysis and machine learning  
754 - robotics research group, University of Oxford, 2002.

755 Choudrey, R. A. and Roberts, S. J.: Variational mixture of Bayesian independent component analyzers., *Neural Comput.*,  
756 15(1), 213–252, <https://doi.org/10.1162/089976603321043766>, 2003.

757 Cornes, R. C., van der Schrier, G., van den Besselaar, E. J. M. and Jones, P. D.: An Ensemble Version of the E-OBS  
758 Temperature and Precipitation Data Sets, *J. Geophys. Res. Atmos.*, 123(17), 9391–9409,  
759 <https://doi.org/10.1029/2017JD028200>, 2018.

760 Dal Zilio, L., Hetényi, G., Hubbard, J. and Bollinger, L: Building the Himalaya from tectonic to earthquake scales. *Nature*  
761 *Reviews Earth & Environment*, 2, 251–268, <https://doi.org/10.1038/s43017-021-00143-1>, 2021.

762 van Dam, T., Collilieux, X., Wuite, J., Altamimi, Z. and Ray, J.: Nontidal ocean loading: amplitudes and potential effects in

763 GPS height time series, *J. Geod.*, 86(11), 1043–1057, <https://doi.org/10.1007/s00190-012-0564-5>, 2012.

764 Dill, R.: Hydrological model LSDM for operational Earth rotation and gravity field variations, Deutsches  
765 GeoForschungsZentrum GFZ, <https://doi.org/10.2312/gfz.b103-08095>, 2008.

766 Dill, R. and Dobslaw, H.: Numerical simulations of global-scale high-resolution hydrological crustal deformations, *J. Geophys.*  
767 *Res. Solid Earth*, 118(9), 5008–5017, <https://doi.org/10.1002/jgrb.50353>, 2013.

768 Dong, D., Fang, P., Bock, Y., Webb, F., Prawirodirdjo, L., Kedar, S. and Jamason, P.: Spatiotemporal filtering using principal  
769 component analysis and Karhunen-Loeve expansion approaches for regional GPS network analysis, *J. Geophys. Res.*, 111(B3),  
770 <https://doi.org/10.1029/2005JB003806>, 2006.

771 Faccenna, C., Becker, T. W., Miller, M. S., Serpelloni, E. and Willett, S. D.: Isostasy, dynamic topography, and the elevation  
772 of the Apennines of Italy, *Earth and Planetary Science Letters*, 407, 163–174, <https://doi.org/10.1016/j.epsl.2014.09.027>,  
773 2014a.

774 Faccenna, C., Becker, T. W., Auer, L., Billi, A., Boschi, L., Brun, J. P., Capitanio, F. A., Funicello, F., Horvath, F., Jolivet,  
775 L., Piromallo, C., Royden, L., Rossetti, F. and Serpelloni, E.: Mantle dynamics in the Mediterranean, *Rev. Geophys.*, 52(3),  
776 283–332, <https://doi.org/10.1002/2013RG000444>, 2014b.

777 Faranda, D., Sato, Y., Saint-Michel, B., Wiertel, C., Padilla, V., Dubrulle, B. and Daviaud, F.: Stochastic chaos in a turbulent  
778 swirling flow., *Phys. Rev. Lett.*, 119(1), 014502, <https://doi.org/10.1103/PhysRevLett.119.014502>, 2017.

779 Fu, Y. and Freymueller, J. T.: Seasonal and long-term vertical deformation in the Nepal Himalaya constrained by GPS and  
780 GRACE measurements, *J. Geophys. Res.*, 117(B3), <https://doi.org/10.1029/2011JB008925>, 2012.

781 Fu, Y., Freymueller, J. T. and Jensen, T.: Seasonal hydrological loading in southern Alaska observed by GPS and GRACE,  
782 *Geophys. Res. Lett.*, 39(15), <https://doi.org/10.1029/2012GL052453>, 2012.

783 Gegout, P., Boy, J. P., Hinderer, J. and Ferhat, G.: Modeling and Observation of Loading Contribution to Time-Variable GPS  
784 Sites Positions, in *Gravity, Geoid and Earth Observation: IAG Commission 2: Gravity Field*, Chania, Crete, Greece, 23-27  
785 June 2008, vol. 135, edited by S. P. Mertikas, pp. 651–659, Springer Berlin Heidelberg, Berlin, Heidelberg,  
786 [https://doi.org/10.1007/978-3-642-10634-7\\_86](https://doi.org/10.1007/978-3-642-10634-7_86), , 2010.

787 Ghasemi Khalkhali, S. A., A. Ardalan, A. and Karimi, R.: A time series analysis of permanent GNSS stations in the northwest  
788 network of Iran, *Annals of Geophysics*, 64(2), <https://doi.org/10.4401/ag-8450>, 2021.

789 Gualandi, A. and Liu, Z.: Variational bayesian independent component analysis for insar displacement time-series with  
790 application to central california, USA, *J. Geophys. Res. Solid Earth*, 126(4), <https://doi.org/10.1029/2020JB020845>, 2021.

791 Gualandi, A., Serpelloni, E. and Belardinelli, M. E.: Blind source separation problem in GPS time series, *J. Geod.*, 90(4), 323–  
792 341, <https://doi.org/10.1007/s00190-015-0875-4>, 2016.

793 Gualandi, A., Nichele, C., Serpelloni, E., Chiaraluce, L., Anderlini, L., Latorre, D., Belardinelli, M. E. and Avouac, J. P.:  
794 Aseismic deformation associated with an earthquake swarm in the northern Apennines (Italy), *Geophys. Res. Lett.*, 44(15),  
795 7706–7714, <https://doi.org/10.1002/2017GL073687>, 2017a.

796 Gualandi, A., Perfettini, H., Radiguet, M., Cotte, N. and Kostoglodov, V.: GPS deformation related to  
797 the *M* 7.3, 2014, Papanaoa earthquake (Mexico) reveals the aseismic behavior of the Guerrero seismic  
798 gap, *Geophys. Res. Lett.*, 44(12), 6039–6047, <https://doi.org/10.1002/2017GL072913>, 2017b.

799 He, M., Shen, W., Pan, Y., Chen, R., Ding, H. and Guo, G.: Temporal-Spatial Surface Seasonal Mass Changes and Vertical  
800 Crustal Deformation in South China Block from GPS and GRACE Measurements., *Sensors*, 18(1),  
801 <https://doi.org/10.3390/s18010099>, 2017.

802 He, X., Yu, K., Montillet, J.-P., Xiong, C., Lu, T., Zhou, S., Ma, X., Cui, H. and Ming, F.: GNSS-TS-NRS: An Open-Source  
803 MATLAB-Based GNSS Time Series Noise Reduction Software, *Remote Sens (Basel)*, 12(21), 3532,  
804 <https://doi.org/10.3390/rs12213532>, 2020.

805 Henrion, E., Masson, F., Doubre, C., Ulrich, P. and Meghraoui, M.: Present-day deformation in the Upper Rhine Graben  
806 from GNSS data, *Geophysical Journal International*, 223(1), 599–611, <https://doi.org/10.1093/gji/ggaa320>, 2020

807 Herring, T. A., King, R. W., Floyd, M. A., and McClusky, S. C.: Introduction to GAMIT/GLOBK, Release 10.7, 2018.  
808 Retrieved from [http://geoweb.mit.edu/gg/Intro\\_GG.pdf](http://geoweb.mit.edu/gg/Intro_GG.pdf)

809 Hou, Z., Guo, Z. and Du, J.: Analysis of the regional GNSS coordinate time series by ICA-weighted spatio-temporal filtering,  
810 *J. Earth Syst. Sci.*, 128(7), 191, <https://doi.org/10.1007/s12040-019-1214-6>, 2019.

811 Huffman, G.J., Stocker, E.F., Bolvin, D.T., Nelkin, E.J. and Jackson Tan: GPM IMERG Final Precipitation L3 1 day 0.1  
812 degree x 0.1 degree V06, Edited by Andrey Savtchenko, Greenbelt, MD, Goddard Earth Sciences Data and Information  
813 Services Center (GES DISC), Accessed: [04-27-2022], 10.5067/GPM/IMERGDF/DAY/06, 2019.

814 Hyvärinen, A. and Oja, E.: A Fast Fixed-Point Algorithm for Independent Component Analysis, *Neural Comput.*, 9(7), 1483–  
815 1492, <https://doi.org/10.1162/neco.1997.9.7.1483>, 1997.

816 Jiang, W., Ma, J., Li, Z., Zhou, X. and Zhou, B.: Effect of removing the common mode errors on linear regression analysis of  
817 noise amplitudes in position time series of a regional GPS network & a case study of GPS stations in Southern California,  
818 *Adv. Space Res.*, 61(10), 2521–2530, <https://doi.org/10.1016/j.asr.2018.02.031>, 2018.

819 Klos, A., Olivares, G., Teferle, F. N., Hunegnaw, A. and Bogusz, J.: On the combined effect of periodic signals and colored  
820 noise on velocity uncertainties, *GPS Solut.*, 22(1), 1, <https://doi.org/10.1007/s10291-017-0674-x>, 2018.

821 Klos, A., Dobsław, H., Dill, R. and Bogusz, J.: Identifying the sensitivity of GPS to non-tidal loadings at various time  
822 resolutions: examining vertical displacements from continental Eurasia, *GPS Solut.*, 25(3), 89, <https://doi.org/10.1007/s10291->



823 021-01135-w, 2021.

824 Kositsky, A. P. and Avouac, J. P.: Inverting geodetic time series with a principal component analysis-based inversion method,  
825 *J. Geophys. Res.*, 115(B3), <https://doi.org/10.1029/2009JB006535>, 2010.

826 Koulali, A. and Clarke, P. J.: Effect of antenna snow intrusion on vertical GPS position time series in Antarctica, *J. Geod.*,  
827 94(10), 101, <https://doi.org/10.1007/s00190-020-01403-6>, 2020.

828 Kreemer, C. and Blewitt, G.: Robust estimation of spatially varying common-mode components in GPS time-series, *J. Geod.*,  
829 95(1), 13, <https://doi.org/10.1007/s00190-020-01466-5>, 2021.

830 Kumar, U., Chao, B. F. and Chang, E. T. Y.: What causes the common-mode error in array GPS displacement fields: case  
831 study for taiwan in relation to atmospheric mass loading, *Earth and Space Science*, 7(11),  
832 <https://doi.org/10.1029/2020EA001159>, 2020.

833 Larochelle, S., Gualandi, A., Chanard, K. and Avouac, J. P.: Identification and extraction of seasonal geodetic signals due to  
834 surface load variations, *J. Geophys. Res. Solid Earth*, <https://doi.org/10.1029/2018JB016607>, 2018.

835 Li, W., Li, F., Zhang, S., Lei, J., Zhang, Q., Yuan, L.: Spatiotemporal Filtering and Noise Analysis for Regional GNSS Network  
836 in Antarctica Using Independent Component Analysis. *Remote Sens (Basel)*, 11(4), 386, <https://doi.org/10.3390/rs11040386>,  
837 2019.

838 Lin, L. I.: A concordance correlation coefficient to evaluate reproducibility., *Biometrics*, 45(1), 255–268,  
839 <https://doi.org/10.2307/2532051>, 1989.

840 Liu, B., Dai, W., Peng, W. and Meng, X.: Spatiotemporal analysis of GPS time series in vertical direction using independent  
841 component analysis, *Earth Planet. Sp.*, 67(1), 189, <https://doi.org/10.1186/s40623-015-0357-1>, 2015.

842 Liu, B., Dai, W. and Liu, N.: Extracting seasonal deformations of the Nepal Himalaya region from vertical GPS position time  
843 series using Independent Component Analysis, *Adv. Space Res.*, <https://doi.org/10.1016/j.asr.2017.02.028>, 2017.

844 Masson, C., Mazzotti, S. and Vernant, P.: Precision of continuous GPS velocities from statistical analysis of synthetic time  
845 series, *Solid Earth*, 10(1), 329–342, <https://doi.org/10.5194/se-10-329-2019>, 2019.

846 Mey, J., Scherler, D., Wickert, A. D., Egholm, D. L., Tesauro, M., Schildgen, T. F. and Strecker, M. R.: Glacial isostatic uplift  
847 of the European Alps. *Nature Communications*, 7(1), 13382. <https://doi.org/10.1038/ncomms13382>, 2016.

848 Ming, F., Yang, Y., Zeng, A. and Zhao, B.: Spatiotemporal filtering for regional GPS network in China using independent  
849 component analysis, *J. Geod.*, 91(4), 419–440, <https://doi.org/10.1007/s00190-016-0973-y>, 2017.

850 Nikolaidis, R.: Observation of geodetic and seismic deformation with the Global Positioning System, PhD thesis, Univ. of  
851 Calif., San Diego, 2002.

852 Nocquet, J.-M., Sue, C., Walpersdorf, A., Tran, T., Lenôtre, N., Vernant, P., Cushing, M., Jouanne, F., Masson, F., Baize, S.,  
853 Chéry, J., van der Beek, P. A.: Present-day uplift of the western Alps. *Scientific Reports*, 6(1), 28404.  
854 <https://doi.org/10.1038/srep28404>, 2016.

855 Palano, M., Pezzo, G., Serpelloni, E., Devoti, R., D’Agostino, N., Gandolfi, S., Sparacino, F., Anderlini, L., Poluzzi, L.,  
856 Tavasci, L., Macini, P., Pietrantonio, G., Riguzzi, F., Antoncicchi, I., Ciccone, F., Rossi, G., Avallone, A. and Selvaggi, G.:  
857 Geopositioning time series from offshore platforms in the Adriatic Sea., *Sci. Data*, 7(1), 373, [https://doi.org/10.1038/s41597-](https://doi.org/10.1038/s41597-020-00705-w)  
858 [020-00705-w](https://doi.org/10.1038/s41597-020-00705-w), 2020.

859 Pan, Y., Chen, R., Ding, H., Xu, X., Zheng, G., Shen, W., Xiao, Y. and Li, S.: Common Mode Component and Its Potential  
860 Effect on GPS-Inferred Three-Dimensional Crustal Deformations in the Eastern Tibetan Plateau, *Remote Sens (Basel)*, 11(17),  
861 1975, <https://doi.org/10.3390/rs11171975>, 2019.

862 Pintori, F., Serpelloni, E., Longuevergne, L., Garcia, A., Faenza, L., D’Alberto, L., Gualandi, A. and Belardinelli, M. E.:  
863 Mechanical response of shallow crust to groundwater storage variations: inferences from deformation and seismic observations  
864 in the eastern southern alps, italy, *J. Geophys. Res. Solid Earth*, 126(2), <https://doi.org/10.1029/2020JB020586>, 2021.

865 Riddell, A. R., King, M. A. and Watson, C. S.: Present-day vertical land motion of Australia from GPS observations and  
866 geophysical models, *J. Geophys. Res. Solid Earth*, <https://doi.org/10.1029/2019JB018034>, 2020.

867 Rodell, M., Houser, P. R., Jambor, U., Gottschalck, J., Mitchell, K., Meng, C. J., Arsenault, K., Cosgrove, B., Radakovich, J.,  
868 Bosilovich, M., Entin, J. K., Walker, J. P., Lohmann, D. and Toll, D.: The global land data assimilation system, *Bull. Amer.*  
869 *Meteor. Soc.*, 85(3), 381–394, <https://doi.org/10.1175/BAMS-85-3-381>, 2004.

870 Serpelloni, E., Faccenna, C., Spada, G., Dong, D. and Williams, S. D. P.: Vertical GPS ground motion rates in the Euro-  
871 Mediterranean region: New evidence of velocity gradients at different spatial scales along the Nubia-Eurasia plate boundary,  
872 *J. Geophys. Res. Solid Earth*, 118(11), 6003–6024, <https://doi.org/10.1002/2013JB010102>, 2013.

873 Serpelloni, E., Vannucci, G., Anderlini, L. and Bennett, R. A.: Kinematics, seismotectonics and seismic potential of the eastern  
874 sector of the European Alps from GPS and seismic deformation data, *Tectonophysics*, 688, 157–181,  
875 <https://doi.org/10.1016/j.tecto.2016.09.026>, 2016.

876 Serpelloni, E., Pintori, F., Gualandi, A., Scocimarro, E., Cavaliere, A., Anderlini, L., Belardinelli, M. E. and Todesco, M.:  
877 Hydrologically Induced Karst Deformation: Insights From GPS Measurements in the Adria-Eurasia Plate Boundary Zone, *J.*  
878 *Geophys. Res. Solid Earth*, 123(5), 4413–4430, <https://doi.org/10.1002/2017JB015252>, 2018.

879 Silverii, F., Pulvirenti, F., Montgomery-Brown, E. K., Borsa, A. A. and Neely, W. R.: The 2011-2019 Long Valley Caldera  
880 inflation: New insights from separation of superimposed geodetic signals and 3D modeling, *Earth and Planetary Science*  
881 *Letters*, 569, 117055, <https://doi.org/10.1016/j.epsl.2021.117055>, 2021.

882 Sternai, P., Sue, C., Husson, L., Serpelloni, E., Becker, T. W., Willett, S. D., Faccenna, C., Di Giulio, A., Spada, G., Jolivet,

883 L., Valla, P., Petit, C., Nocquet, J.-M., Walpersdorf, A. and Castellort, S.: Present-day uplift of the European Alps: Evaluating  
884 mechanisms and models of their relative contributions, *Earth-Science Reviews*, 190, 589–604,  
885 <https://doi.org/10.1016/j.earscirev.2019.01.005>, 2019.

886 Tan, W., Dong, D. and Chen, J.: Application of independent component analysis to GPS position time series in Yunnan  
887 Province, southwest of China, *Advances in Space Research* 69(11), 4111-4122, <https://doi.org/10.1016/j.asr.2022.03.016>.

888 Tape, C., Musé, P., Simons, M., Dong, D. and Webb, F.: Multiscale estimation of GPS velocity fields. *Geophysical Journal  
889 International* 179, 945–971. <https://doi.org/10.1111/j.1365-246X.2009.04337.x>, 2009.

890 Tiampo, K. F., Rundle, J. B., Klein, W., Ben-Zion, Y. and McGinnis, S.: Using eigenpattern analysis to constrain seasonal  
891 signals in southern california, *Pure appl. geophys.*, 161(9–10), <https://doi.org/10.1007/s00024-004-2545-y>, 2004.

892 Tian, Y. and Shen, Z.: Extracting the regional common-mode component of GPS station position time series from dense  
893 continuous network, *J. Geophys. Res. Solid Earth*, 121(2), 1080–1096, <https://doi.org/10.1002/2015JB012253>, 2016.

894 Tian, Y. and Shen, Z.: Correlation weighted stacking filtering of common-mode component in GPS observation network, *Acta  
895 Seismologica Sinica*, 33(2), 198-208, 2011.

896 Vicente-Serrano, S. M. and López-Moreno, J. I.: Nonstationary influence of the North Atlantic Oscillation on European  
897 precipitation, *J. Geophys. Res.*, 113(D20), <https://doi.org/10.1029/2008JD010382>, 2008.

898 Wdowinski, S., Bock, Y., Zhang, J., Fang, P. and Genrich, J.: Southern California permanent GPS geodetic array: Spatial  
899 filtering of daily positions for estimating coseismic and postseismic displacements induced by the 1992 Landers earthquake,  
900 *J. Geophys. Res.*, 102(B8), 18057–18070, <https://doi.org/10.1029/97JB01378>, 1997.

901 Yan, J., Dong, D., Bürgmann, R., Materna, K., Tan, W., Peng, Y. and Chen, J.: Separation of sources of seasonal uplift in  
902 china using independent component analysis of GNSS time series, *J. Geophys. Res. Solid Earth*, 124(11), 11951–11971,  
903 <https://doi.org/10.1029/2019JB018139>, 2019.

904 Yuan, P., Jiang, W., Wang, K. and Sneeuw, N.: Effects of spatiotemporal filtering on the periodic signals and noise in the GPS  
905 position time series of the crustal movement observation network of china, *Remote Sens (Basel)*, 10(9), 1472,  
906 <https://doi.org/10.3390/rs10091472>, 2018.

907 Zhang, K., Wang, Y., Gan, W. and Liang, S.: Impacts of local effects and surface loads on the common mode error filtering  
908 in continuous GPS measurements in the northwest of yunnan province, china., *Sensors*, 20(18),  
909 <https://doi.org/10.3390/s20185408>, 2020.

910 Zhu, Z., Zhou, X., Deng, L., Wang, K. and Zhou, B.: Quantitative analysis of geophysical sources of common mode component  
911 in CMONOC GPS coordinate time series, *Adv. Space Res.*, 60(12), 2896–2909, <https://doi.org/10.1016/j.asr.2017.05.002>,  
912 2017.